Surrogate-based aerodynamic shape optimization for delaying airfoil dynamic stall using Kriging regression and infill criteria

Vishal Raul, Leifur Leifsson *

Department of Aerospace Engineering, Iowa State University, Ames, IA, 50011, USA

ARTICLE INFO

ABSTRACT

The dynamic stall phenomenon is characterized by the formation of a leading-edge vortex, which is responsible for adverse aerodynamic forces and moments adversely impacting the structural strength and life of a system. Aerodynamic shape optimization (ASO) provides a cost-effective approach to delay or mitigate the dynamic stall characteristics. Unfortunately, ASO requires multiple evaluations of accurate but time-consuming computational fluid dynamics (CFD) simulations to produce optimum designs rendering the optimization process computationally costly. The current work proposes a surrogate-based optimization (SBO) technique to alleviate the computational burden of ASO to delay and mitigate the deep dynamic stall characteristics of airfoils. In particular, the Kriging regression surrogate model is used for approximating the objective and constraint functions. The airfoil geometry is parametrized using six PARSEC parameters. The objective and constraint functions are evaluated with the unsteady Reynolds-averaged Navier-Stokes equations with a C-grid mesh topology and Menter's shear stress transport turbulence model. The approach is demonstrated on a vertical axis wind turbine airfoil at a Reynolds number of 135,000 and a Mach number of 0.1 undergoing a sinusoidal oscillation with a reduced frequency of 0.05. The surrogate model is constructed with 60 initial samples and further refined with 20 infill samples using expected improvement. The generated surrogate model is validated with the normalized root mean square error based on 20 test data samples. The refined surrogate model is utilized for finding the optimal design using multi-start gradient-based search. The optimal airfoil has a higher thickness, larger leading-edge radius, and an aft camber compared to the baseline. These geometric shape changes delay the dynamic stall angle by over 3° and reduces the severity of the pitching moment coefficient fluctuation. Finally, global sensitivity analysis is conducted on the optimal design using Sobol' indices revealing the most influential shape variables and their interaction effects impacting the airfoil dynamic stall characteristics.

© 2021 Elsevier Masson SAS. All rights reserved.

1. Introduction

Wind energy is a sustainable energy resource and is proving to be one of the most economical methods of unsubsidized energy generation [1]. The wind energy industry has been driven by horizontal axis wind turbines (HAWTs) due to their high efficiency in steady winds. In recent years, vertical axis wind turbines (VAWTs) have acquired growing interest with its suitability to urban and offshore applications [2]. VAWTs have several advantages over HAWTs. For example, VAWTs are simple in design, self-starting, omnidirectional, less noisy, inexpensive to construct and have lower operational and maintenance costs [3]. VAWTs, however, suffer from an inherent complex unsteady aerodynamic phenomenon known as dynamic stall when operating at a low tip-speed ratio ($TSR \leq 5$). In VAWTs, dynamic stall arises from rapid changes in the angle of attack perceived by each blade in every rotational cycle [4,5], generating adverse loading which significantly impacts the blades, hub, tower structure, power output, and the turbine life. An accurate understanding and consideration of dynamic stall is a major priority in the design process of VAWTs to improve their performance and structural life. Recently, the wind turbine industry has directed significant efforts towards modeling the dynamic stall and dynamic loading to improve turbine life [6,7].

In the case of dynamic stall, aerodynamic shape optimization (ASO) can be used to passively mitigate adverse dynamic loading over aerodynamic surfaces using accurate computational fluid

Nomenclature

$\tilde{f}$	Favre mean of the flow variable	
α	Angle of attack	deg
α_{ds}	Dynamic stall angle of attack	deg
α_{ms}	Moment stall angle of attack	deg
β_{TE}	Airfoil trailing edge wedge angle	deg
θ	Vector of Kriging hyperparameters	
$\Delta\alpha$	Delay in dynamic stall angle	deg
δ_{ij}	Kronecker delta	
$\mathbf{x}$	Vector of design variables	
$\mathbf{x}_{lb}$	Vector containing lower bounds on design variables	
$\mathbf{x}_{ub}$	Vector containing upper bounds on design variables	
μ_t	Turbulent eddy viscosity	Pa s
ω	Rotational rate	$\frac{rad}{s}$
ρ_∞	Free-stream density	kg/m^3
τ_{ij}	Viscous stress tensor component	Pa
θ_z	Azimuth angle	rad
θ_{TE}	Airfoil trailing edge directional angle	deg
A	Amplitude of oscillations	deg
a^s	PARSEC surface coefficient	
c	Chord length	
c_d	Sectional drag coefficient, $\frac{d}{\frac{1}{2}\rho_\infty U_\infty^2 S}$	
c_l	Sectional lift coefficient, $\frac{l}{\frac{1}{2}\rho_\infty U_\infty^2 S}$	
c_m	Sectional pitching moment coefficient, $\frac{m}{\frac{1}{2}\rho_\infty U_\infty^2 Sc}$	
$c_{d_{err}}$	Estimated error in average drag coefficient	d.c.
$c_{d_{RE}}$	Richardson extrapolation estimate of average drag coefficient per cycle	d.c.
d	Drag force	N
dt	Timestep	s
f	Scalar objective function	
f_v	Favre average of flow variable	
g	Inequality constraint function	
H	Total enthalpy per unit mass	J/kg
h	Equality constraint function	
J	Scalar function	
k	Turbulent kinetic energy	m^2/s^2
k_r	Reduced frequency, $\frac{\omega c}{2U_\infty}$	
l	Lift force	N
L	Airfoil lower surface	
m	Pitching moment	Nm
M_∞	Free-stream Mach number	
m_{max}	Airfoil maximum camber	
n	Number of design variables	
n_s	Number of design samples	
n_t	Number of test data samples	
p	Static pressure	Pa
R_{LE}	Airfoil leading edge radius	
Re	Reynolds number	
S	Reference area	m^2
t_{max}	Airfoil maximum thickness	
t_{off}	Airfoil trailing edge offset	
t_{TE}	Airfoil trailing edge thickness	
TSR	Tip-speed ratio	
u	Velocity component in Cartesian system	m/s
U	Airfoil upper surface	
U_∞	Free-stream velocity	m/s
X	Airfoil surface crest x-coordinate	
x_c	Non-dimensional chordwise location	
$x_{m_{max}}$	Non-dimensional chordwise location of m_{max}	
$x_{t_{max}}$	Non-dimensional chordwise location of t_{max}	
y	Function of interest	
y^+	Non-dimensionalized first layer cell thickness	
Z	Airfoil surface crest z-coordinate	
z	z-coordinate of airfoil section	
Z_{xx}	Second-order derivative of airfoil surface	
d.c.	Drag counts, $\Delta c_d = 0.0001$	

dynamics (CFD) models. Surrogate-based optimization (SBO) [8] provides an efficient approach to alleviate the computational cost of ASO. In this paper, SBO is used to efficiently find optimum shapes for delaying dynamic stall occurrence over VAWT airfoils. In particular, the Kriging regression surrogate [9] with the expected improvement (EI) [9,10] infill criteria is used to represent the design objective function and constraints with respect to the airfoil design parameters. The airfoil shapes are parameterized with the PARSEC method [11]. The accuracy of the surrogate model is adaptively enhanced with the EI infill criteria and validated with the normalized root mean square error (NRMSE) metric. Optimum airfoil shapes are found by optimizing the surrogate model with the multi-start gradient-based optimization (GBO) method [12]. Additionally, global sensitivity analysis of the design objective with respect to the design variables is performed with Sobol' indices [13] to provide information on how the airfoil design parameters affect the dynamic stall characteristics. The proposed approach is applied to a VAWT airfoil, however, it can be applied to other aerospace systems undergoing dynamic stall.

The remainder of this paper is structured as follows. The next section presents a literature review on ASO, SBO and their applications to the dynamic stall problem. The subsequent section describes the SBO approach used in this work, which includes the problem statement, problem formulation, optimization algorithm and Sobol' sensitivity analysis. The following section describes the test case and the computational model setup used for evaluating airfoil dynamic stall. The next section presents the results of the

optimization and sensitivity analysis studies. Finally, conclusions and suggestions for future work are given.

2. Background

Dynamic stall phenomenon frequently occurs on helicopter rotors [14], maneuvering aircraft [15], wind turbines [16–18], and bio-inspired micro air vehicles (MAVs)/unmanned air vehicles (UAVs) [19–23]. Thus, considerable research has been done experimentally and computationally to understand dynamic stall physics and airfoil shape dependencies by studying a sinusoidally oscillating airfoil in a uniform flow [14,24–27]. Furthermore, significant research has been conducted on alternatives to mitigate or control dynamic stall via active and passive control systems [28–33]. Application of these approaches can increase the system mass and may require an auxiliary control system, which may increase the complexity and cost of the wind turbine system. Therefore, these approaches may not be economically viable for VAWT applications.

ASO is a method to design aerodynamic surfaces for optimum performance. ASO was first applied by Hicks et al. [34] for airfoil drag minimization of nonlifting, transonic airfoils in inviscid flow. Since then it has become an essential component of aerodynamic design to improve the performance of various engineered systems, such as aircraft [35,36], cars [37], wind turbines [38,39], trains [40], and compressors [41,42]. In the case of dynamic stall, ASO can be used to mitigate adverse dynamic loading thereby enhancing and optimizing the performance of aerodynamic surfaces. With the development of computer technology, shape optimization studies can

be performed using accurate CFD simulations, although, there are several challenges to this task.

ASO is an iterative process that requires multiple model evaluations to produce an optimum design. The GBO method is a widely used technique in ASO. A major bottleneck in this approach is the large computational cost in evaluating the objective function and constraints using accurate CFD models and determining their gradient information with respect to the design variables. This computational cost increases quickly with the number of design variables. In the adjoint-based method [43], sensitivities of the objective and constraint functions with respect to the design variables are used with GBO technique to efficiently find the optimum design. In particular, the adjoint-based design approach is nearly independent of the number of design variables, which renders the approach highly scalable to large design spaces [44]. The adjoint-based ASO method is currently widely considered the state-of-the-art for solving aerodynamic design optimization problems.

Examples of applications of adjoint-based ASO include the following. Jameson et al. [43] applied the continuous adjoint method for cruise drag reduction of the Boing 747-200 wing using a Reynolds-averaged Navier-Stokes (RANS) based CFD model. Dhert et al. [39] used the adjoint method for ASO of wind turbine blades with 240 shape variables for maximizing the torque of the NREL VI wind turbine. Lei et al. [45] applied an adjoint approach for aerodynamic optimization of civil aircraft with a wing-mounted engine, including 462 wing shape and three engine position variables for minimizing the drag coefficient at the nominal cruise condition.

Most ASO applications are used for steady-state flow problems because of the high computational cost associated with unsteady flow problems. ASO for the mitigation of dynamic stall adverse effects have received limited attention due to the complex flow physics and high computational cost. Recent efforts, however, have produced shape optimization strategies for two-dimensional (2d) [46–50] and three-dimensional (3d) [2,51] dynamic stall problems.

The adjoint method with the GBO approach has been frequently used for dynamic stall optimization cases chiefly because of the inexpensive gradient calculation. Examples of such work follow. Wong et al. [46] used a discrete adjoint method with a 2d steady state RANS solver for minimizing the drag coefficient of the VR-7 airfoil in steady state condition and then tested the optimized shape in unsteady sinusoidal pitching motion to see its effects under dynamic stall conditions. Nadarajah et al. [47] developed time accurate discrete and continuous adjoint methods for time-averaged drag minimization through shape optimization of the RAE 2822 airfoil operating at varied flow conditions. Mani et al. [48] used the time dependent adjoint approach for reducing peak pitching moments of the SC1095 helicopter airfoil during the pitching cycle. A sliding mesh strategy with time accurate continuous adjoint method was implemented by Economon et al. [52] for airfoil shape optimization in unsteady flow. Apart from adjoint method, Wang et al. [49,50] used GBO approach with sequential quadratic programming (SQP), unsteady RANS (URANS) and the class shape transformation method for airfoil parameterization to alleviate drag and pitching moment divergence during dynamic stall cycle on rotor airfoils.

There is a possibility that the shape obtained from the GBO method is a local optimum [53]. For instance, GBO starts with a design and moves towards an optimum by using local gradient information. Since, the GBO search may only cover a part of the design space, the optimum solution obtained by this approach can be a local optimum [54]. Genetic algorithms (GAs) [55] are more likely to find a global optimum than GBO methods. In general, GA-based search requires multiple model evaluations in the entire design space, which can be computationally time-consuming, and even prohibitive, if the CFD model is called directly, especially

for high-dimensional design problems. GA-based methods do not use adjoint information.

Several works on GA-based ASO approaches have been reported. Anderson et al. [54] used GA for high-efficiency missile geometry design for multiple-objective problems. Quagliarella et al. [56] and Yamamoto et al. [57] applied GA for designing transonic airfoils. Ma et al. [2] used the multi-island GA for airfoil shape optimization to improve the power performance of VAWT with 3d URANS simulations at moderate tip-speed ratios.

The SBO method [8,58] can be used to alleviate the computational cost of ASO problems. In this approach, a surrogate model (also called a metamodel) is constructed of the objective function within the design space using an approximation method. The surrogate model is fast to evaluate and can be used in lieu of the physics-based simulation model within the optimization loop. Occasionally, the simulation model is evaluated to gather new data to update or correct the surrogate model. Once the surrogate model has been constructed, it can be searched using GBO or GA method.

Few works have presented the application of SBO to ASO of unsteady problems. Tang et al. [59] used Kriging surrogate modeling technique for the shape optimization of cycloidal rotor airfoil in unsteady flow. Wang et al. [51] successfully applied a Kriging-based SBO for finding optimal rotor shapes for a helicopter application. The SBO method has been used successfully in turbomachinery shape optimization problems [41,42,60], where the computational cost of each evaluation can be as high as in dynamic stall CFD simulations.

3. Surrogate-based shape optimization

This section presents the methodology of the shape optimization using surrogate models for delaying airfoil dynamic stall. In particular, the section describes the problem statement and optimum design problem formulation providing details on the design variables and the objective and constraint function formulations. The optimization algorithm is described in detail, including the Kriging regression surrogate modeling, infill criteria, and the surrogate model validation as well as the sensitivity analysis based on Sobol' indices.

3.1. Problem statement

In this study, a straight-blade fixed-pitch VAWT (called the Darrieus-type wind turbine) is considered. When the VAWT rotates, the relative velocity perceived by the airfoil section changes continuously with respect to the azimuthal location of the blade. This type of motion is often referred to as the Darrieus motion [61]. The magnitude of the angle of attack (α) variation in the Darrieus motion without velocity induction from the rotor can be expressed, in terms of the tip-speed ratio (TSR) and the azimuthal angle (θ_z) as [61]

$$\alpha(TSR, \theta_z) = \arctan\left(\frac{\sin(\theta_z)}{TSR + \cos(\theta_z)}\right). \quad (1)$$

The variation of the normalized angle of attack ($\frac{\alpha(TSR,\theta_z)}{\alpha_{max}}$) for several tip-speed ratios in Darrieus motion is shown in Fig. 1a against the sine curve. In VAWTs, dynamic stall typically occurs at a low tip-speed ratio ($TSR \leq 5$). The variation of the normalized angle of attack in the Darrieus motion is similar to the sine curve motion. Thus, the angle of attack variation in VAWTs can be approximated as an airfoil in a sinusoidal pitching motion in a stationary frame of reference. Considering the similarity of these types of motions it is likely that there is a similarity with regards to the dynamic stall mechanics [5]. Moreover, the dynamic stall
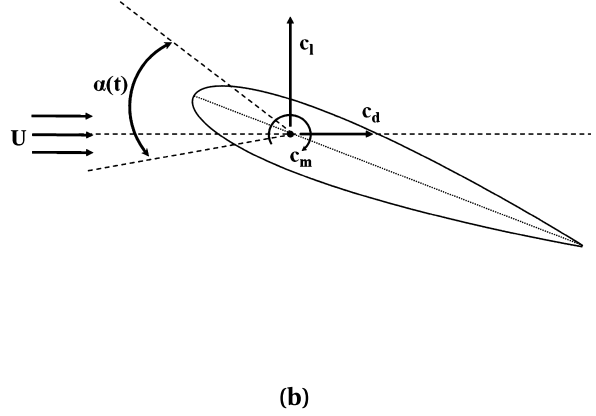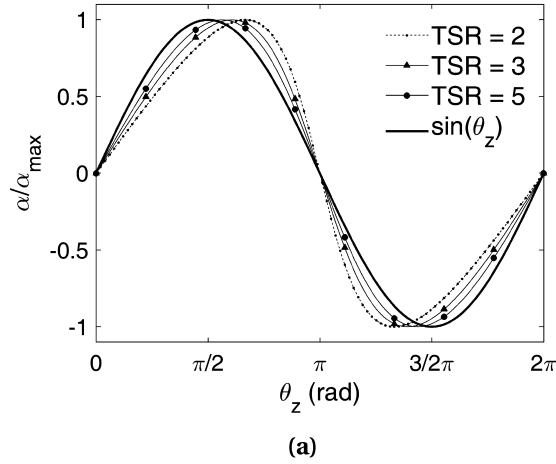
Fig. 1. Parameters for describing the airfoil oscillating motion and response: (a) normalized blade angle of attack variation ($\frac{\alpha(TSR,\theta_z)}{\alpha_{max}}$) with varying tip-speed ratios TSR in Darrieus motion, and (b) the force and moment coefficients at the quarter chord of an airfoil in uniform flow.

Table 1
Dynamic stall motion and flow parameters [63].

Parameters	Values	Units
α_m	10°	deg
A	15°	deg
ω	3.403	rad/s
k_r	0.05	-
Re	135,000	-

phenomenon has traditionally been studied with a sinusoidal oscillating motion, hence, a large number of experimental data sets are available for comparison and validation. Therefore, this study considers the simple sinusoidal pitching motion instead of the realistic but complicated Darrieus motion of the VAWT blade.

Airfoil sinusoidal oscillating motion in a freestream flow is shown in Fig. 1b. The pitching motion of the airfoil is described using the angle of attack as a function of time (t) as

$$\alpha(t) = \alpha_m + A \sin(\omega t), \tag{2}$$

where α_m, A, and ω represent the mean angle of attack, the amplitude of oscillation, and the rotational rate, respectively. The reduced frequency, k_r, is another important parameter relating time unit, t, of rotation to the time scale of the flow passing over airfoil section. The reduced frequency is defined as

$$k_r = \frac{\omega c}{2U_\infty}, \tag{3}$$

where c is the chord length and U_∞ is the freestream speed.

Dynamic stall can be categorized as a light stall and a deep stall [14] based on the angle of attack variation beyond the static stall angle (α_{ss}) of the airfoil during pitching oscillation [62]. The VAWT airfoils undergo deep dynamic stall at lower TSR values, causing a severe variation in the aerodynamic loads. Accordingly, in this study the deep dynamic stall case from Lee et al. [63] is considered. The details of the airfoil motion parameters and flow conditions are given in Table 1.

3.2. Optimum design problem formulation

The current design problem of mitigating the dynamic stall occurrence through airfoil shape optimization can be transcribed to a general mathematical optimization problem which will include an objective function to maximize the performance of an airfoil subjected to design constraints. The standard optimum design model is written as

$$\min_{\mathbf{x}} \ f(\mathbf{x})$$

$$s.t. \ h_j(\mathbf{x}) = 0; \quad j = 1, 2, ..., m \tag{4}$$

$$g_i(\mathbf{x}) \leq 0; \quad i = 1, 2, ..., p$$

$$\mathbf{x}_{lb} \leq \mathbf{x} \leq \mathbf{x}_{ub}$$

where $f(\mathbf{x})$ is a scalar objective function, $\mathbf{x} = [x_1, x_2, ..., x_n]^T \in D \subset \mathbb{R}^n$ is the design variable vector and D is the design space. The airfoil design is subjected to m equality constraints $h_j(\mathbf{x}) = 0$ and p inequality constraints $g_i(\mathbf{x}) \leq 0$. The inequality constraints also include bounds on the design variable vector as $\mathbf{x}_{lb} \leq \mathbf{x} \leq \mathbf{x}_{ub}$, where $\mathbf{x}_{lb}$ and $\mathbf{x}_{ub}$ are the lower and upper bounds, respectively.

One of the objectives of the current study is to improve the understanding of how the airfoil parameters affect the dynamic stall mitigation. The PARSEC airfoil parameterization [64] offers a set of design variables that directly control the airfoil characteristics, such as the leading edge radius, thickness, and trailing edge wedge angle [11]. Unlike other parameterization techniques, like bump functions [65], B-spline [66] or free-form deformation [67], the PARSEC parameters have a specific meaning which can be appealing to airfoil designers.

In PARSEC, the upper and lower surface of an airfoil are described as [64]

$$z_s = \sum_{i=0}^{6} a_i^s x_c^{i-\frac{1}{2}}, \quad s = U, L \tag{5}$$

where z_s is the z coordinate of the upper or the lower curves, x_c is the non-dimensional chordwise location ($0 \leq x_c \leq 1$), and a_i^S are the undetermined coefficients. The letter s denotes calculation for the upper (U) or the lower (L) surface of the airfoil. The PARSEC airfoil geometry parameters are shown in Fig. 2. Table 2 shows the design variables used in the PARSEC parameterization. A total of 12 parameters define an airfoil with a unit chord length. The first four parameters in Table 2 are separate for the upper and the lower surfaces whereas the last four parameters are common between both of them. In this work, the trailing-edge offset (t_{off}) and the trailing-edge thickness (t_{TE}) are considered to be zero for both surfaces. Since the dynamic stall characteristics are strongly affected by airfoil upper surface. In the current study, the lower surface parameters are kept constant and based on the baseline airfoil (NACA0012) aside from the lower surface leading edge radius R_L. The upper and lower surface leading edge radiuses are designated by one variable ($R_{LE} = R_U = R_L$) to get a better under-
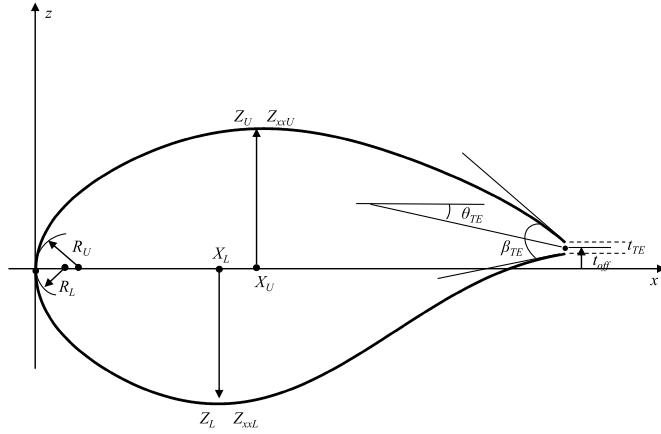
Fig. 2. The PARSEC airfoil geometry parameters.

Table 2
PARSEC design variables.

Design variables	Description	Units
X	Surface crest x coordinate	-
Z	Surface crest z coordinate	-
Z_{xx}	Second-order derivative at X, $\frac{d^2 z}{dx^2}\|_{x=X}$	-
R_{LE}	Leading edge radius	-
θ_{TE}	Trailing edge directional angle	deg
β_{TE}	TE wedge angle	deg
t_{off}	Trailing edge offset	-
t_{TE}	Trailing edge thickness	-

Table 3
Design variables with their bounds for upper airfoil surface.

Design variables	Upper bound	Lower bound	Units
X_U	0.5011	0.2733	-
Z_U	0.09	0.054	-
Z_{xx_U}	−0.4036	−0.6726	-
R_{LE}	0.0222	0.0104	-
θ_{TE_U}	−7.0294	−11.7156	deg
β_{TE_U}	5.8803	3.52818	deg

standing of the effect of the leading-edge radius on the dynamic stall.

The aforementioned conditions reduce the 12 design variables to only six variables and the design variable vector is written as

$$\mathbf{x} = [X_U, Z_U, Z_{xx_U}, R_{LE}, \theta_{TE_U}, \beta_{TE_U}]^T. \tag{6}$$

The design variables and their respective bounds are presented in Table 3 where the variable bounds are selected to allow a larger modification to the objective function magnitude without producing an atypical shape of the airfoil.

The objective of this work is to find an airfoil shape which mitigates the risk of dynamic stall by reducing sudden aerodynamic load variations, while at the same time delaying the occurrence of the dynamic stall point. This objective can be achieved by delaying the formation of the dynamic stall vortex on the airfoil surface which is the cause of sudden divergence observed in the drag and pitching moment coefficients. Thus, the optimization problem formulation can be defined as

$$\min_{\mathbf{x}} \quad f(\mathbf{x}) = \left(\frac{\sum_{i=1}^{N} c_{d_i}(\mathbf{x})}{J(c_{d0})} \right) + \left(\frac{\sum_{i=1}^{N} |c_{m_i}(\mathbf{x})|}{J(c_{m0})} \right) \tag{7}$$

$$s.t. \quad g = \alpha_{ds0} + \Delta\alpha - \alpha_{ds}(\mathbf{x}) \leq 0 \tag{8}$$

$$\mathbf{x}_{lb} \leq \mathbf{x} \leq \mathbf{x}_{ub} \tag{9}$$

where $J(c_{d0}) = \sum_{i=1}^{N}(c_{d0})_i$, $J(c_{m_0}) = \sum_{i=1}^{N} |(c_{m0})_i|$, $c_d(\mathbf{x})$, $c_m(\mathbf{x})$, and $\alpha_{ds}(\mathbf{x})$ represent the time variant drag coefficient, pitching moment coefficient and dynamic stall point of the airfoil shape during dynamic stall cycle; subscript '0' represents the base airfoil parameters; $\Delta\alpha$ denotes the minimum delay in the dynamic stall angle required for optimum design, and N denotes the number of physical timesteps in each pitching cycle. The value of N is depends on simulation timestep and total cycle time. In this study, only the upstroke part of the pitching cycle is considered where the formation of the dynamic stall vortex causes a divergence in the drag and pitching moment coefficients.

3.3. Optimization algorithm

The different steps of optimization algorithm (shown in Fig. 3) are implemented with a python script which calls different modules of the optimization algorithm to construct and sequentially refine the Kriging regression surrogate model with expected improvement as the infill criteria. First, the initial training sample database is generated with a Latin hypercube sampling (LHS) sampling plan [68]. Then, the airfoil shape for each design sample is generated using the PARSEC parameterization technique (cf. Sec. 3.2). The shape coordinates are then used to generate the computational mesh which is then used with CFD solver for design evaluation. Note that in this study only the upstroke of the pitching cycle is simulated where the dynamic stall vortex formation occurs. To avoid transients from affecting the CFD results, the airfoil is initially started in a down-stroke and then in an upstroke. The results from the upstroke are used for the computation of the objective and the constraint function. All initial samples are evaluated similarly.

The acquired observations are used to construct two separate surrogate models, one for the objective and another for the constraint function. The global accuracy of constructed surrogate models are validated using the NRMSE metric (cf. Sec. 3.3.4) over the entire design space using a testing data set. If the surrogate models satisfy the accuracy criteria, then they are passed to the optimizer as well as for the sensitivity analysis (cf. Sec. 3.4). In case the surrogate models do not satisfy the accuracy criteria, an infill point is determined based on the EI infill criteria (cf. Sec. 3.3.3) to improve surrogate model's accuracy. The infill point is evaluated with the CFD module and added to the initial sample database to construct new surrogate models. This process is iterated until the surrogate models satisfy the accuracy criteria. The above optimization algorithm has some similarity with the efficient global optimization (EGO) [10] algorithm. The EGO approach uses a stopping criteria based on percentage of expected improvement whereas the proposed optimization algorithm uses surrogate model accuracy as a stopping criteria. The details of each optimization module are discussed in following subsections.

3.3.1. Sampling plan

The LHS method [68] is used to generate the initial sampling plan in this study. LHS was first proposed by McKay et al. [68] as an alternative to simple random sampling to improve convergence and accuracy of the Monte Carlo simulation [68]. LHS is based on a Latin square design where one sample is placed in each row and column. A Latin hypercube is the multidimensional extension of the Latin square to sample points in multiple hyperplanes [69]. The basic idea in LHS is to separate a sampling point distribution which is close to the probability density function (PDF) [68]. This is done by stratification, which divides the cumulative probability distribution of 0 to 1 in equal intervals. Then, a sample is taken from each interval randomly and the input probability distribution is recreated. The LHS method provides a good distribution of sample points over the design domain ensuring that the entire range
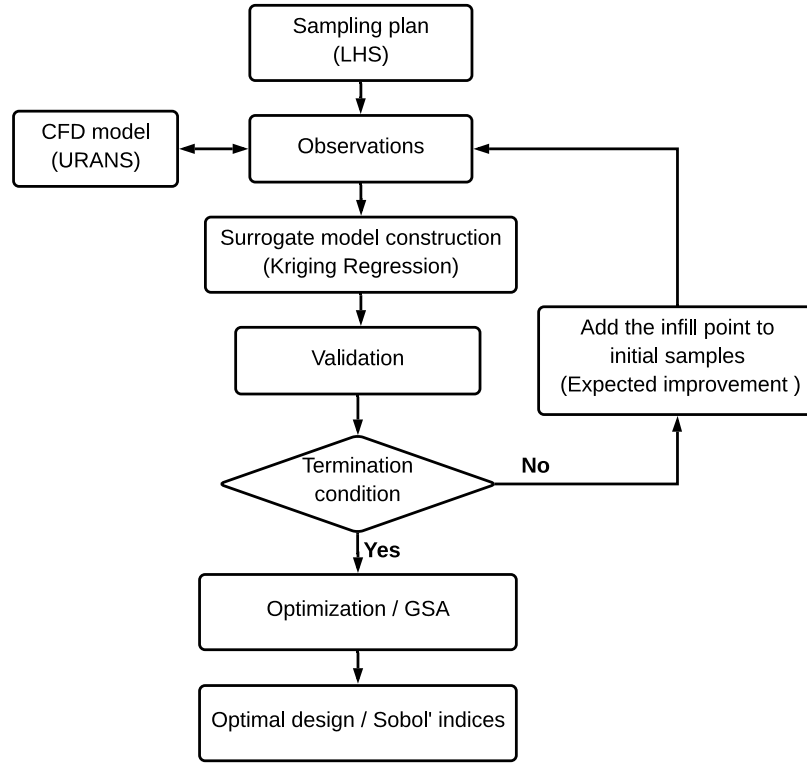
Fig. 3. A flowchart of the surrogate-based optimal design and global sensitivity analysis (GSA).

of the design variables are represented in the sampling plan. In the present study, six design variables are selected for representing airfoil shape (see Sec. 3.2). According to Gu et al. [70] and Shi et al. [71] a number of samples equal to three times the number of design variables are needed at a minimum for the construction of reasonably accurate surrogate models. However, it is desirable to use a larger number of samples than the minimum for higher accuracy of the initially constructed surrogate model. Thus, considering the long time required for each sample evaluation, the number of initial sampling points is taken to be ten times the number of variables.

3.3.2. Surrogate modeling using Kriging regression

Kriging regression [9] is an extension of regular Kriging [72]. Kriging is an interpolation method widely used in SBO for noise free data sets [72]. Kriging approximates the observed response as a combination of a global trend function and a local variation from the global trend as [72]

$$y(\mathbf{x}) = G(\mathbf{x}) + Z(\mathbf{x}), \tag{10}$$

where $y(\mathbf{x})$ is the function of interest, $G(\mathbf{x})$ is a polynomial trend function, and $Z(\mathbf{x})$ is a realization of a normally distributed Gaussian random process with a zero mean, variance σ^2, and non-zero covariance [72].

The global trend function is a product of two vectors given as

$$G(\mathbf{x}) = \mathbf{g}^T(\mathbf{x})\boldsymbol{\beta}, \tag{11}$$

where

$$\mathbf{g}^T(\mathbf{x}) = [g_0(\mathbf{x}), g_1(\mathbf{x}), .., g_{n-1}(\mathbf{x})], \tag{12}$$

is the regression basis functions ($n \leq n_s$ with number of samples as n_s and number of design variables as n) and the regression coefficients

$$\boldsymbol{\beta} = [\beta_0, \beta_1, .., \beta_{n-1}]^T. \tag{13}$$

In regular Kriging, the global trend function is typically taken as constant, which yields $\mathbf{g} = 1$ and $\boldsymbol{\beta}$ a scalar value. In this study $G(\mathbf{x})$ is considered as constant.

The function $Z(\mathbf{x})$ provides a localized variation to the global trend function for a set of sampled data $\mathbf{x}^1, \mathbf{x}^2, ..., \mathbf{x}^{n_s}$ over the design domain D where any given sample is $\mathbf{x}^i \in D \subset \mathbb{R}^n$. Sample points are assumed to be correlated with each other using a Gaussian basis function as [72]

$$R(\mathbf{x}^i, \mathbf{x}^j) = \exp\left[-\sum_{k=1}^{n} \theta_k |x_k^i - x_k^j|^2 \right], \tag{14}$$

where x_k^i and x_k^j are the kth components of any two sample data $\mathbf{x}^i$ and $\mathbf{x}^j$, and θ_k is the kth unknown correlation parameter of $\boldsymbol{\theta} = [\theta_1, \theta_2, ..., \theta_n]^T$, allowing for a variation in width of the basis function. Using the basis function, the covariance of the sampled points is [72]

$$Cov[\mathbf{x}^i, \mathbf{x}^j)] = \sigma^2 \mathbf{R}([R(\mathbf{x}^i, \mathbf{x}^j)]), \tag{15}$$

where $\mathbf{R}$ is a $n_s \times n_s$ symmetric matrix with $\mathbf{R}_{ij} = R(\mathbf{x}^i, \mathbf{x}^j)$.

The Kriging predictor $\hat{y}(\mathbf{x}_u)$ at an untried location $\mathbf{x}_u$ in the design domain is given by [72]

$$\hat{y}(\mathbf{x}_u) = \mathbf{g}^T \hat{\boldsymbol{\beta}} + \mathbf{r}^T(\mathbf{x}_u)\mathbf{R}^{-1}(\mathbf{y} - \mathbf{G}\hat{\boldsymbol{\beta}}), \tag{16}$$

where $\mathbf{y}$ is the column vector of length n_s containing the responses at the sample points, $\mathbf{G}$ is a column vector of length n_s filled with ones when $G(\mathbf{x})$ is considered constant. The vector $\mathbf{r}^T(\mathbf{x}_u) = [R(\mathbf{x}_u, \mathbf{x}^1), R(\mathbf{x}_u, \mathbf{x}^2), ..., R(\mathbf{x}_u, \mathbf{x}^{n_s})]$ is the correlation vector between the known observed points $(\mathbf{x}^1, \mathbf{x}^2, ..., \mathbf{x}^{n_s})$ and the new sample point $\mathbf{x}_u$. The vector $\hat{\boldsymbol{\beta}}$ in (16) is a maximum likelihood estimation (MLE) of $\boldsymbol{\beta}$ and is evaluated as

$$\hat{\beta} = \frac{\mathbf{G}^T \mathbf{R}^{-1} \mathbf{y}}{\mathbf{G}^T \mathbf{R}^{-1} \mathbf{G}}. \tag{17}$$

A Kriging model is fitted to the given sample data by optimizing correlation parameters θ using MLE function. In this work, the concentrated ln-likelihood function is used for estimation of hyperparameters given by [69]

$$l(\theta) = -\frac{n_s}{2} \ln(\hat{\sigma}^2) - \frac{1}{2} \ln |\mathbf{R}|, \tag{18}$$

where $\hat{\sigma}^2$ is a MLE of the Gaussian process variance and is given as

$$\hat{\sigma}^2 = \frac{(\mathbf{y} - \mathbf{G}\beta)^T \mathbf{R}^{-1} (\mathbf{y} - \mathbf{G}\beta)}{n_s}. \tag{19}$$

The optimum value of θ can be found by maximizing the ln-likelihood function using a GA. The crucial property of the Kriging model is its ability to provide an error estimate at unsampled points, which can be used with various infill strategies [69] for improving the surrogate model.

The Kriging method is formulated based on the assumption that the objective function to be approximated is accurate (with no errors), smooth and continuous in the design domain. Typical engineering objective functions are noisy due to the errors involved in numerical modeling. The objective function encountered in a dynamic stall simulation can include errors from the computational simulation when the airfoil oscillates in the separated flow region. This can cause an error in the Kriging approximation when many design points are added closely to find the optimum design. In such a situation, Kriging regression can be used to handle the noisy data [9].

For this study, a Kriging regression surrogate model is used for approximating the objective and constraint functions. The noise filtration capability of Kriging regression is achieved by adding a regression constant λ to the diagonal terms of the Kriging correlation matrix $\mathbf{R}$ which then becomes $\mathbf{R} + \lambda\mathbf{I}$, where $\mathbf{I}$ is the identity matrix. The Kriging regression predictor is now given as [9]

$$\hat{y}_r(\mathbf{x}_u) = \mathbf{g}^T \hat{\beta}_r + \mathbf{r}^T(\mathbf{x}_u)(\mathbf{R} + \lambda\mathbf{I})^{-1}(\mathbf{y} - \mathbf{G}\hat{\beta}_r), \tag{20}$$

where

$$\hat{\beta}_r = \frac{\mathbf{G}^T (\mathbf{R} + \lambda\mathbf{I})^{-1} \mathbf{y}}{\mathbf{G}^T (\mathbf{R} + \lambda\mathbf{I})^{-1} \mathbf{G}}, \tag{21}$$

and estimated variance of Gaussian process $\hat{\sigma}_r^2$ is given as

$$\hat{\sigma}_r^2 = \frac{(\mathbf{y} - \mathbf{G}\hat{\beta}_r)^T (\mathbf{R} + \lambda\mathbf{I})^{-1} (\mathbf{y} - \mathbf{G}\hat{\beta}_r)}{n_s}, \tag{22}$$

where the subscript 'r' denotes regression. Similar to regular Kriging, Kriging regression can be fitted to the sampled data by maximizing the ln-likelihood function given as

$$l(\theta, \lambda) = -\frac{n_s}{2} \ln(\hat{\sigma}^2) - \frac{1}{2} \ln |(\mathbf{R} + \lambda\mathbf{I})|, \tag{23}$$

where the hyperparameters λ and θ are determined using a global optimizer such as a GA. In this work, differential evolution (DE) [73], a stochastic population-based global optimization method, is used for determining the hyperparameters. In particular, the DE algorithm offered by SciPy [74] is used for the optimization task. Kriging regression is described in detail in Forrester et al. [9].

3.3.3. Infill criteria

The surrogate model developed by Kriging or Kriging regression is an approximation of the objective function. The search for the minimum depends on the accuracy of the surrogate model. The surrogate model's accuracy can be improved by adding more points in design space in addition to the initial sampling plan. For this study, the expected improvement (EI) [10,69] is used as an infill criterion to balance global exploration and local exploitation of the objective function. For Kriging, the expected improvement can be calculated by using the mean $\hat{y}$ and the mean square error $\hat{s}^2$ as [69]

$$\mathbb{E}[I(\mathbf{x}_u)]$$
$$= \begin{cases} (y_{\min} - \hat{y})\Phi\left(\frac{y_{\min} - \hat{y}}{\hat{s}}\right) + \hat{s}\phi\left(\frac{y_{\min} - \hat{y}}{\hat{s}}\right) & \text{when } \hat{s} > 0 \\ 0 & \text{when } \hat{s} = 0 \end{cases} \tag{24}$$

where Φ and φ are the cumulative distribution function and the probability density function, respectively. The new point will be added at the location of maximum $E[I(\mathbf{x})]$. The Kriging mean square error [69] is

$$\hat{s}^2(\mathbf{x}_u) = \hat{\sigma}^2 \left[1 - \mathbf{r}^T \mathbf{R}^{-1} \mathbf{r} + \frac{1 - \mathbf{G}^T \mathbf{R}^{-1} \mathbf{r}}{\mathbf{G}^T \mathbf{R}^{-1} \mathbf{G}} \right]. \tag{25}$$

The computation of the expected improvement in (24) with the mean square error in (25) can be implemented as

$$\mathbb{E}[I(\mathbf{x}_u)] = (y_{\min} - \hat{y})\left[\frac{1}{2} + \frac{1}{2} \operatorname{erf}\left(\frac{y_{\min} - \hat{y}}{\hat{s}\sqrt{2}} \right) \right]$$
$$+ \hat{s}\frac{1}{2\pi} \exp\left[\frac{-(y_{\min} - \hat{y})^2}{\hat{s}} \right]. \tag{26}$$

Note that the error $\hat{s}^2$ is zero at the sample points. The expected improvement should also be zero at sampled points such that model does not revaluate at already sampled points. Hence, $\Phi() = 0$ and $\mathbb{E}[I(\mathbf{X})] = 0$ when $\hat{s} = 0$. The expected improvement function with no possibility of resampling guarantees global convergence [69].

It should also be noted that Kriging regression can not be directly used with the expected improvement infill criteria in (26). This is mainly because of the error associated with the noise in the sampled data. The error $\hat{s}^2$ is always present in the Kriging regression model at all the points and does not reduce to zero as in the Kriging model. This gives rise to the possibility of resampling with non-zero $\mathbb{E}[I(\mathbf{x}_u)]$, potentially stalling the search process with no guarantee of obtaining global optimum [9].

This problem is solved by redefining the Kriging error, thereby eliminating error due to the noise in the model [9,69]. This method is known as re-interpolation and is covered in detail in Forrester et al. [9]. The redefined Kriging mean squared error with re-interpolation is given as [9]

$$\hat{s}_{ri}^2(\mathbf{x}) = \hat{\sigma}_{ri}^2 \left[1 - \mathbf{r}^T \mathbf{R}^{-1} \mathbf{r} + \frac{1 - \mathbf{G}^T \mathbf{R}^{-1} \mathbf{r}}{\mathbf{G}^T \mathbf{R}^{-1} \mathbf{G}} \right], \tag{27}$$

where the variance $\hat{\sigma}_{ri}^2$ with re-interpolation is given by [9]

$$\hat{\sigma}_{ri}^2 = \frac{(\mathbf{y} - \mathbf{G}\hat{\beta}_r)^T (\mathbf{R} + \lambda\mathbf{I})^{-1} \mathbf{R} (\mathbf{R} + \lambda\mathbf{I})^{-1} (\mathbf{y} - \mathbf{G}\hat{\beta}_r)}{n_s}. \tag{28}$$

The subscript 'ri' denotes re-interpolation. Now the Kriging error calculation (27) reduces to zero at the known sample points allowing the expected improvement to find the global optimum of the model. The error $\hat{s}_{ri}$ is then used with (26) to calculate the EI magnitude in the design domain.

Finally, an infill point can be found by maximizing the function (26) with a global optimizer such as a GA. In this work, DE [73], implemented in SciPy [74], is used for determining the infill point by maximizing the EI function (26) with re-interpolation.

3.3.4. Surrogate model validation

The global accuracy of the surrogate model should be validated before using it in the optimization or GSA process. For this study, the normalized root mean squared error (NRMSE) is used for the surrogate model validation. The NRMSE is defined as

$$\text{NRMSE} = \frac{\sqrt{\sum_{i=1}^{n_t} \frac{(y_t^i - \hat{y}_t^i)^2}{n_t}}}{(y_{\max} - y_{\min})_I},$$ (29)

where y_t^i and $\hat{y}_t^i$ represent the responses from the CFD model evaluation and surrogate model prediction at the ith test sample, respectively. The response value y is either the objective function or the constraint function value for their respective error estimations. The n_t is the number of testing data samples. The denominator of $(y_{\max} - y_{\min})_I$ represents the difference of the maximum and the minimum response values in the initial sample data set. In this work, NRMSE $\leq 10\%$, with a fixed budget of 20 infill samples, is considered as acceptable criteria for the surrogate modeling.

3.4. Global sensitivity analysis by Sobol' indices

An important objective of this study is to determine the critical parameters that affect the dynamic stall characteristics. Sensitivity analysis (SA) is the study of predicting uncertainty in a model output due to the uncertainty in the model inputs [75]. SA of the dynamic stall objective function would provide the quantification of the sensitivities of individual variables to the dynamic stall mitigation. This information would be important to the designer for identifying critical regions in the design space and simplifying the model by only considering the essential input design variables.

SA can be categorized as being either local or global. Local SA quantifies the rate of change of the model output due to small changes in the model input. Local SA relies on the calculation of derivatives which are specific to the current point and does not capture the interaction with other design variables and are often not valid for nonlinear models [75]. Global sensitivity analysis (GSA) focuses on the model output uncertainty over the entire ranges of the input variables providing information of how variations in the input variables affect the model output. The Sobol' analysis is a widely used GSA method [13,76] and yields the first-order and the total-effect of the input design variables. In this work, Sobol' indices [13] are used for the GSA.

Sobol's method uses a variance decomposition to calculate the Sobol' indices. Consider the function $Y = f(\mathbf{x})$ being the model response with $\mathbf{x}$ as the vector of n input variables. The model response can be decomposed as [76]

$$f(\mathbf{x}) = f_0 + \sum_{i=1}^{n} f_i(x_i) + \sum_{1 \leq i \leq j \leq n} f_{ij}(x_i, x_j) + \ldots$$
$$+ f_{12\ldots k}(x_1, x_2, \ldots, x_n),$$ (30)

where f_0 is a constant, f_i are first-order functions, f_{ij} are second-order functions and so on. The above decomposition has 2^n finite number of terms. Sobol' proved that all the terms of the decomposition are orthogonal in pairs [76], i.e., $\int f(x_i) f(x_j) \, dx_i dx_j = 0$ considering that each term in the above expansion has a zero mean. Hence, these terms can be calculated using a conditional expectation of the model output Y as

$$f_0 = \mathbb{E}(Y),$$ (31)

$$f_i = \mathbb{E}(Y|x_i) - \mathbb{E}(Y),$$ (32)

$$f_{ij} = \mathbb{E}(Y|x_i, x_j) - f_i - f_j - \mathbb{E}(Y).$$ (33)

The conditional expectation $\mathbb{E}(Y|x_i)$ can be calculated empirically by separating x_i from the domain and averaging the value of $(Y|x_i)$. If $\mathbb{E}(Y|x_i)$ has a large variation across x_i then the variable x_i is believed to be important. Therefore, the variance in $\mathbb{E}(Y|x_i)$ is a measure of sensitivity. Hence, with further modifications the terms in the decomposition (30) can be written as [76]

$$\mathbb{V}(Y) = \sum_{i}^{n} V_i + \sum_{i}^{n} \sum_{i<j}^{n} V_{ij} + \ldots + V_{12\ldots n},$$ (34)

where V_i is $\mathbb{V}[\mathbb{E}(Y|x_i)]$ and $\mathbb{V}(Y)$ represents the total variance in the model response Y. The Sobol' indices can be obtained by dividing (34) by $\mathbb{V}(Y)$ to obtain

$$1 = \sum_{i}^{n} S_i + \sum_{i}^{n} \sum_{i<j}^{n} S_{ij} + \ldots + S_{12\ldots n},$$ (35)

where S_i represents the first-order Sobol' index given by [76]

$$S_i = \frac{V_i}{\mathbb{V}(Y)}.$$ (36)

The total-effect Sobol' index is given as [76]

$$S_{T_i} = 1 - \frac{\mathbb{V}(\mathbb{E}(Y|\mathbf{x}_{\sim i}))}{\mathbb{V}(Y)},$$ (37)

where $\mathbf{x}_{\sim i}$ represents the set of all variables except x_i. The total-effect index S_{T_i} accommodates the total contribution of x_i to the model output variation $\mathbb{V}(Y)$. This includes the first-order effect plus higher order effects due to interactions with other variables. With availability of the Sobol' indices (S_i and S_{T_i}) the interaction effects of x_i with other variables can be computed by $S_{T_i} - S_i$ which provides added information about the design variable interactions.

The Sobol' indices can be computed with a Monte Carlo-based numerical procedure given by Saltelli [77]:

(1) Generate a $(N, 2n)$ matrix of random numbers in design variable bound where n is the number of design variables and N represents the number of samples used for the SA. Get two matrices **A** and **B**, each with size (N, n). Sobol' recommended a quasi-random sequence for the random number generation [76]. LHS is an another technique which can be used for the sample generation [75]. Hence, LHS sampling with uniform distribution is utilized for sampling design variables.
(2) Build matrix $\mathbf{C}_i$ of size (N, n), such that all the columns are from **B** except the ith column which is from **A**.
(3) Obtain three column vectors (Y_A, Y_B and Y_{C_i}) of size $(N, 1)$ by evaluating the model at design variables from matrices **A**, **B** and $\mathbf{C}_i$ where

$$Y_A = f(\mathbf{A}), \; Y_B = f(\mathbf{B}), \; Y_{C_i} = f(\mathbf{C}_i).$$ (38)

(4) Compute the first-order effect S_i and the total-effect S_{T_i} Sobol' indices for the ith design variable by using the following estimators given by Saltelli [76,77] as

$$S_i = \frac{\frac{1}{N} \sum_{j=1}^{N} Y_A^j Y_{C_i}^j - f_0^2}{\frac{1}{N} \sum_{j=1}^{N} (Y_A^j)^2 - f_0^2},$$ (39)

where

$$f_o^2 = \left(\frac{1}{N}\sum_{j=1}^{N} Y_A^j\right)^2, \tag{40}$$

and

$$S_{T_i} = 1 - \frac{\frac{1}{N}\sum_{j=1}^{N} Y_B^j Y_{C_i}^j - f_0^2}{\frac{1}{N}\sum_{j=1}^{N}(Y_A^j)^2 - f_0^2}. \tag{41}$$

Following are some of the properties of Sobol' indices which are useful for the interpretation of the sensitivity results [76]:

(1) By definition $S_{T_i} \geq S_i$. The case of $S_{T_i} = S_i$ implies that the ith (x_i) variable has no interactions with other design variables.
(2) $S_{T_i} - S_i$ represents the degree of the x_i variable involvement in interactions with other variables.
(3) $S_{T_i} = 0$ indicates that x_i does not have any influence on other variables and can be fixed without affecting the variance of model output.
(4) The sum of all S_i is equal to 1 for additive models and $S_i \leq 1$ for non-additive models. The magnitude of $1 - \sum_{i=1}^{n} S_i$ suggests the presence of interactions in the model.
(5) $\sum_{i=1}^{n} S_{T_i}$ is always greater than 1 and $\sum_{i=1}^{n} S_{T_i}$ is equal to 1 only for perfectly additive models.

4. Computational fluid dynamics modeling

This section describes the CFD model setup considered for the current study. First, the governing equations used in the CFD model are described, followed by a description of flow solver and its setup. Then, the computational grid is described, and the results of the grid and time-independence studies are presented. Lastly, the results of a validation study comparing the proposed CFD model against experimental results are presented.

4.1. Governing equations

The current study is performed with URANS as the governing equations. The RANS equations are obtained by the time-averaged Navier-Stokes equations. Averaging removes high-frequency fluctuations, reducing the range of length scales presented in flow. The two types of averaging methods are the classical Reynolds averaging and the mass-weighted averaging, also known as Favre average [78]. The Favre average of any flow variable f_v is given as

$$f_v = \tilde{f} + f'', \tag{42}$$

where $\tilde{f} = \frac{\overline{\rho f}}{\bar{\rho}}$ and f'' are the Favre mean and the Favre fluctuating component, respectively. The Favre average is preferred for a compact compressible flow treatment of the Navier-Stokes equations. The application of the classical and the Favre averaging to the conservation of mass, momentum and energy gives the URANS equations [78]:

$$\frac{\partial \bar{\rho}}{\partial t} + \frac{\partial}{\partial x_i}(\bar{\rho}\tilde{u}_i) = 0, \tag{43}$$

$$\frac{\partial}{\partial t}(\bar{\rho}\tilde{u}_i) + \frac{\partial}{\partial x_j}(\bar{\rho}\tilde{u}_i\tilde{u}_j) = \frac{\partial \bar{p}}{\partial x_i} + \frac{\partial \tilde{\tau}_{ij}}{\partial x_j} - \frac{\partial}{\partial x_j}(\overline{\rho u_i'' u_j''}), \tag{44}$$

$$\frac{\partial}{\partial t}(\bar{\rho}\tilde{H}) + \frac{\partial}{\partial x_i}(\bar{\rho}\tilde{u}_j\tilde{H} + \overline{\rho u'' H''} - k\frac{\partial \bar{T}}{\partial x_j})$$
$$= \frac{\partial \bar{p}}{\partial t} + \frac{\partial}{\partial x_j}(\tilde{u}_i\bar{\tau}_{ij} + \overline{u_i''\tau_{ij}}), \tag{45}$$

where $\rho, p, u_i, T, H,$ and τ_{ij} are the density, pressure, velocity component, temperature, total enthalpy and viscous stress tensor, respectively. The term $-\overline{\rho u_i'' u_j''}$ is referred to as the Reynolds stress, which represents the effects of turbulent fluctuations in fluid flow given by

$$-\overline{\rho u_i'' u_j''} = \mu_t\left(\frac{\partial u_i}{\partial x_j} + \frac{\partial u_j}{\partial x_i} - \frac{2}{3}\frac{\partial u_k}{\partial x_k}\delta_{ij}\right) - \frac{2}{3}\rho k\delta_{ij}, \tag{46}$$

where k is the turbulent kinetic energy, μ_t is the turbulent eddy viscosity, and δ_{ij} is the Kronecker delta function. For the closure of the above URANS equations, Reynolds stress is modeled by one- or two-equation turbulence models.

In this study, Menter shear stress transport (SST) [79] turbulence model is used. The SST model is a two-equation eddy-viscosity turbulence model that blends $k - \omega$ and $k - \epsilon$ models. The SST model has shown acceptable performance for dynamic stall and complete VAWT simulation cases by multiple researchers [5,61,80] to capture separated flow regions.

4.2. Flow solver

The Stanford University Unstructured (SU^2) [81] is utilized in this work as the numerical solver which is capable of solving multi-disciplinary problems governed by partial differential equations (PDEs) in general, unstructured meshes. SU^2 has been validated extensively on a number of fluid problems involving compressible, turbulent flows [81,82]. For unsteady simulations, SU^2 offers a dual time-stepping strategy [81] to achieve high order accuracy in time where the unsteady problem is converted to a steady problem at each physical time step and then solved using the steady-state convergence acceleration techniques.

The dynamic stall simulations in this study are performed using the URANS solver with dual time-stepping strategy, and rigid grid motion. The governing equations are discretized using the finite volume method with the convective flux calculations done using the Jameson-Schmidt-Turkel (JST) scheme [81]. The viscous flux evaluations are assisted by the calculation of the flow variable gradients with the Green-Gauss method [81]. Time discretization is done by the Euler implicit scheme [81] with maximum Courant-Friedrichs-Lewy (CFL) number selected as 4. The two-level Multigrid W-cycle method [81] is also used for convergence acceleration. Finally, the Cauchy convergence criteria [83] is implemented on the drag calculation with 100 elements and Cauchy-epsilon criteria set to 10^{-6}.

4.3. Computational grid

In this study, the grid generation is conducted using the blockMesh utility in OpenFoam [84]. The blockMesh utility generates a mesh of blocks of hexahedral cells. The domain geometry is divided into one or multiple three-dimensional blocks. For the dynamic stall simulation, a C-grid mesh is generated around the airfoil. The mesh is refined near the airfoil surface to capture the boundary layer and the complex flow physics generated during the dynamic stall cycle. The first layer thickness is selected so that $y^+ \leq 0.8$ with a growth ratio of around 1.05. A low y^+ is necessary to capture the onset of dynamic stall vortex accurately. An external boundary is set at 55 chord lengths away from the airfoil to minimize boundary reflection effects. The airfoil surface is set with the no-slip adiabatic wall boundary condition. Fig. 4 shows two views of a coarse computational mesh used for the NACA 0012 airfoil. Finally, the mesh generated by the blockmesh utility is converted to a SU^2 compatible file format.

4.4. Grid and time independence studies

Variations in mesh density can alter the CFD model output which subsequently affects the objective and constraint functions
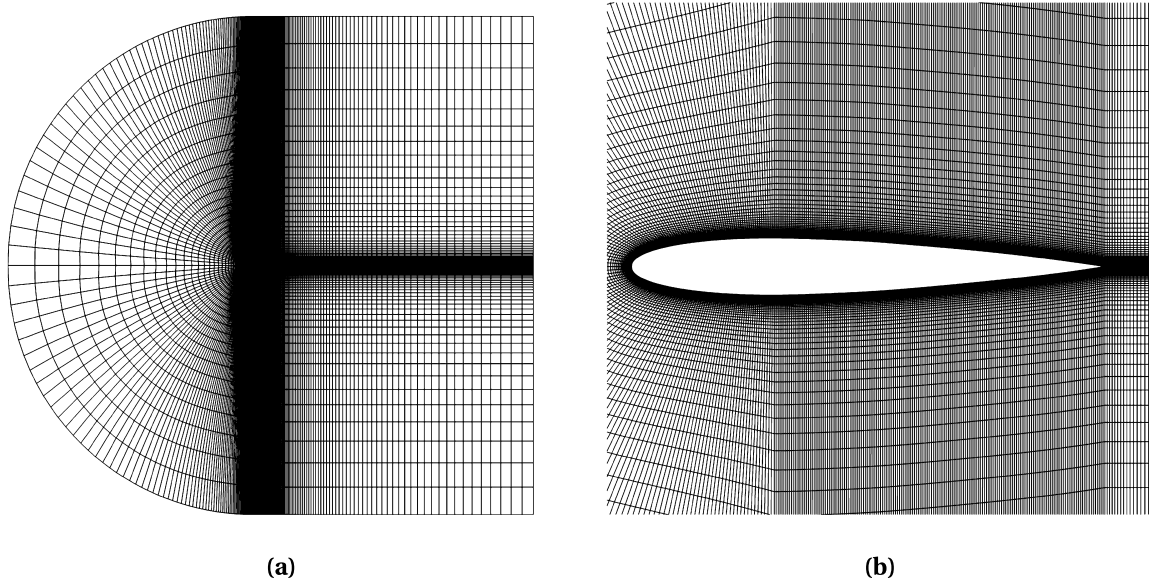
(a)

(b)

Fig. 4. A coarse c-mesh around the NACA 0012 airfoil: (a) the full computational domain and (b) the mesh close to the airfoil.
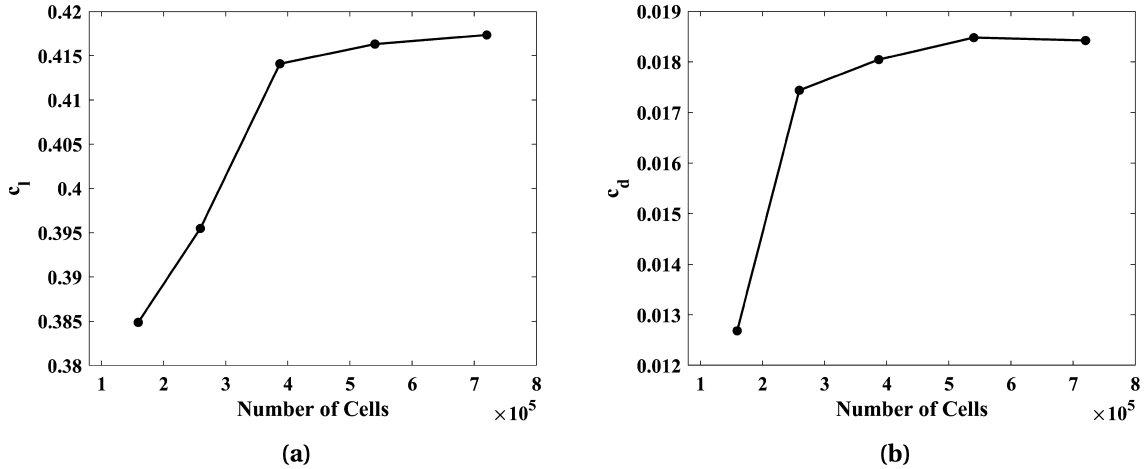

(a)

(b)

Fig. 5. Results of the grid independence study of the NACA 0012 airfoil at Re = 135,000 showing the variation in (a) the lift coefficient, and (b) the drag coefficient.

used in the optimization and GSA. Therefore, grid and time independence studies are conducted to determine efficient spatial and temporal resolutions to capture the flow physics accurately.

A converged computational model is obtained in the following way. Initially, the spatial resolution is obtained with a grid study on a baseline airfoil, the NACA0012 airfoil, at steady-state flow conditions. The selected flow conditions are the same as those considered by Lee et al. [63]. The resulting mesh is used to conduct the time step independence study with an oscillating pitching cycle to determine a physical time step for the URANS simulation. The grid independence study is conducted for a Reynolds number of 135,000, angle of attack of 4°, and turbulence intensity of 0.08% with a RANS solver. The Cauchy convergence criteria on the drag values is set to a Cauchy-epsilon value of 10^{-6} over 100 flow solver iterations. The maximum solver iterations are set to 150,000.

The results of the grid independence study are shown in Fig. 5. Five grids with ascending spatial resolution are selected for the study with $y^+ \leq 0.8$. The three grids with the highest spatial resolution show minimal change in the lift coefficient $\Delta c_l \leq 0.003$ with a drag count variation within 4 d.c. The simulation time requirement for the 387,000 cell mesh is almost three times less than

the simulation time of the highest resolution mesh. Therefore, the mesh with 387,000 cells is selected for this study.

After the selection of appropriate spatial resolution, a time study is executed on the selected mesh to determine the physical time step required for unsteady simulation. The dynamic stall simulations are conducted with the parameters and flow conditions the same as considered in the experimental study done by Lee et al. [63] (see Table 1). The time step independence study is performed with multiple time steps as shown in Table 4.

The selection of the time step is made by using the generalized Richardson extrapolation method [85]. Richardson's extrapolation method obtains a higher-order estimation of the value under consideration from lower-order values. In this work the average drag coefficient per oscillating cycle, $c_{d_{avg}}$, is used for this method. Richardson's extrapolation estimate, $c_{d_{RE}}$, represents the average drag coefficient per cycle at a zero time step (lowest possible), which was found to be 2,108 d.c. Fig. 6 shows the average drag coefficient per cycle versus the time step lengths and their estimated error $c_{d_{err}}$ from the Richardson extrapolation estimate $c_{d_{RE}}$ at each time step. Based on these results, a time step of 0.0015 is selected.
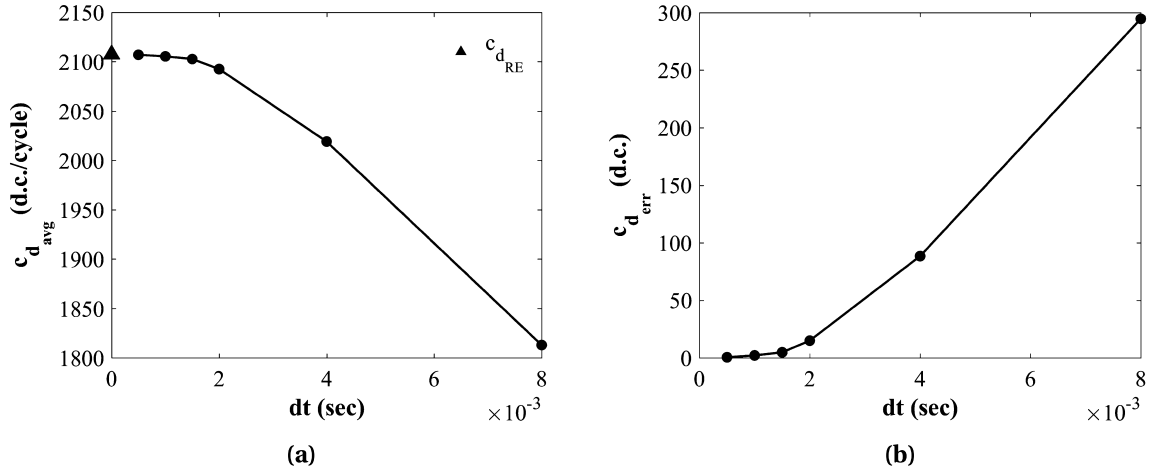
Fig. 6. Results of the time step independence study showing (a) the Richardson extrapolation estimate based on the lower order values, and (b) the estimated error from the Richardson extrapolation.

Table 4
Time step independence study results.

dt (s)	$c_{d_{avg}}$ (d.c./cycle)	Simulation time[*] (hrs/cycle)	$c_{d_{err}} = |c_{d_{avg}} - c_{d_{RE}}|$ (d.c.)
0.008	1,813	39	295.6
0.004	2,019	51	88.4
0.002	2,093	65	14.9
0.0015	2,103	69	4.8
0.001	2,105	78	2.1
0.0005	2,107	99	0.52

[*] Computed on a high performance cluster with 112 processors. Wall-clock time.

Table 5
Comparison of the dynamic stall and moment stall locations for URANS, LES and experiments.

Models	Moment stall	Dynamic stall
URANS [this work]	15.9°	18.7°
LES [86]	17.8°	19.7°
Experiments [63]	17.2°	20.6°

5. Results

This section presents the results of the proposed approach for delaying the dynamics stall over an airfoil. First, the surrogate model construction details, infill process, and surrogate model accuracy are presented. Then, the optimal design and its dynamic stall characteristics are described. Lastly, the results of global sensitivity analysis on constructed surrogate models are presented.

5.1. Surrogate modeling

The surrogate modeling algorithm uses 60 initial LHS samples to construct two separate surrogate models, one for the objective function and the other for the constraint function. For this study $\Delta\alpha = 3°$ is considered in constraint function (8) which denotes the minimum delay in the dynamic stall angle required for optimum design. The surrogate models are validated against 20 test data points generated using a different LHS plan and evaluated with the CFD model. In this study, NRMSE metric is used for the validation. Furthermore, a termination criteria of NRMSE $\leq$ 10% and a fixed budget of 20 infill points is used. The surrogate models are then sequentially improved by adding infill points using the EI infill criteria based on the objective function.

Fig. 8 shows a plot of the NRMSE for the objective and constraint functions change with the number of samples. Both surrogate models satisfy the accuracy criteria well before infill points reach the fixed budget criteria. The constraint function surrogate model shows a higher accuracy than the objective function surrogate model reaching 2.4% and 8.8%, respectively, with 80 sample points (60 initial samples plus 20 infill points). The entire optimization algorithm needed approximately 376,320 CPU hours, considering negligible cost requirements for training surrogate models. Each evaluation with the CFD module is done with 112 cores on a high-performance computing cluster that needs around 4,704 CPU hours. The following sections describe the results of the optimal design and the GSA.
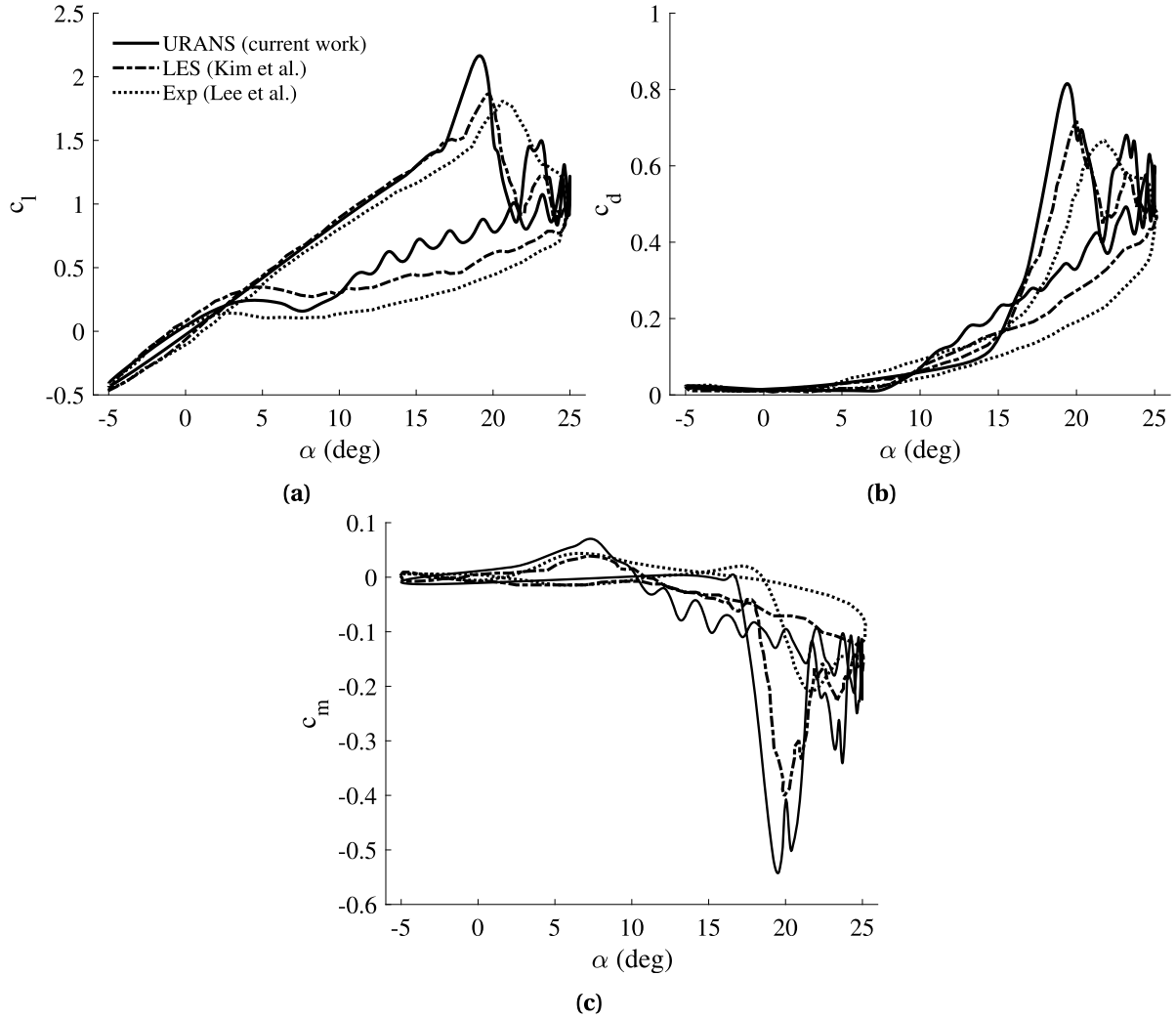
4.5. CFD model validation

The aerodynamic performance of the selected computational mesh configuration is compared against the experimental [63] and LES simulation [86] results using the deep dynamic stall described in Table 1. The computation is performed using the SU^2 URANS solver over 1.5 cycles for validation where the airfoil initially moves in the downstroke cycle from a mean angle (10°) to the lowest angle ($-5°$) and data is collected for the next complete cycle. The addition of the downstroke part of the cycle allows the flow to stabilize from the abrupt change in rotation rate from zero to a finite value at first time step. The entire computation takes 69 hours (wall-clock time) using 7 nodes with 16 cores per node on the high performance computing cluster.

Fig. 7 shows the time dependent aerodynamic loads obtained from the URANS model for the NACA0012 airfoil and compares it to the experimental and LES simulation data. The presented experimental data is a hundred cycle average, whereas LES data is averaged over three cycles. The dynamic stall angles are given in Table 5.

From Fig. 7 it is seen that the URANS model shows a reasonable agreement with the LES model and a qualitative agreement with experimental data. The URANS model captures the moment and dynamic stall locations early in the oscillation cycle. Additionally, the URANS model overpredicts the maximum lift and pitching moment coefficients. The LES model results show a much closer agreement to the experimental results when compared to URANS model. Considering the computational time and resource requirement of the LES model, the URANS model is a practical option for the dynamic stall evaluation of airfoils in the context of optimal design and GSA.

Fig. 7. A comparison of the time dependent aerodynamic coefficients: (a) lift, (b) drag, (c) pitching moment, obtained from the URANS model (current work), LES model [86] and experiments [63] with oscillation cycle parameters $\alpha = 10° + 15° \sin(\omega t)$, $k_r = 0.05$.
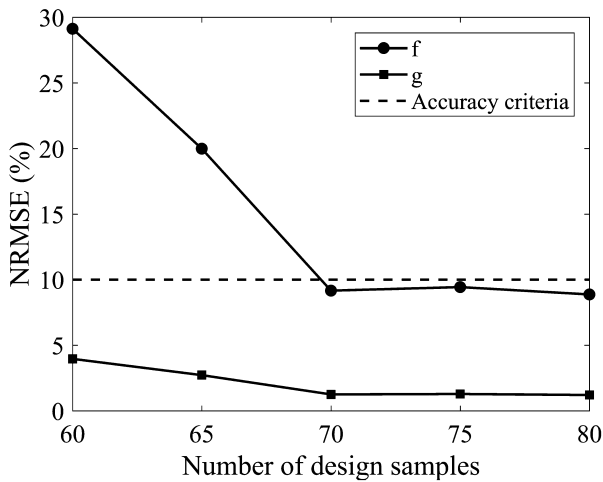

Fig. 8. Surrogate model construction of the objective (f) and constraint (g) functions.

5.2. Optimal design

Once the surrogate models satisfy the accuracy criteria, they are passed to the optimizer to find an optimal design for prob-

lem formulation proposed in Sec. 3.2. In this work, the multi-start gradient-based search algorithm is used to find the optimal design. In particular, the sequential least squares programming (SLSQP) [87] algorithm provided in SciPy [74] is utilized in this work. A total of 240 starting points distributed over the entire design space are obtained using the LHS technique [68]. The best obtained result is taken as the optimal design.

Fig. 9a shows the progression of the optimal shapes obtained at every five infill points. It can be observed that as the surrogate modeling converges, the optimal design converges as well since consecutive optimal shapes show small variations. This can also be observed in Fig. 9b, which shows the L2 norm magnitude between two consecutive optimal designs. For example, the magnitude of the L2 norm at 65th sample is the difference between the optimum shapes with 65 and 60 samples. Additional information of the optimum airfoil shapes is given in Table 6. The shape obtained with 80 sample points is considered as optimum design for this study.

A grid and time independence study is done on the optimum design to ensure that the selected grid and time step are still appropriate for the acquired shape. The same setup and step are utilized for this grid and time study as that of the baseline shape (see Section 4.4). Fig. 10 shows the results of the grid study on the optimized airfoil. The three grids with the highest spatial resolution show minor variation in lift coefficient within $\Delta c_l < 0.003$
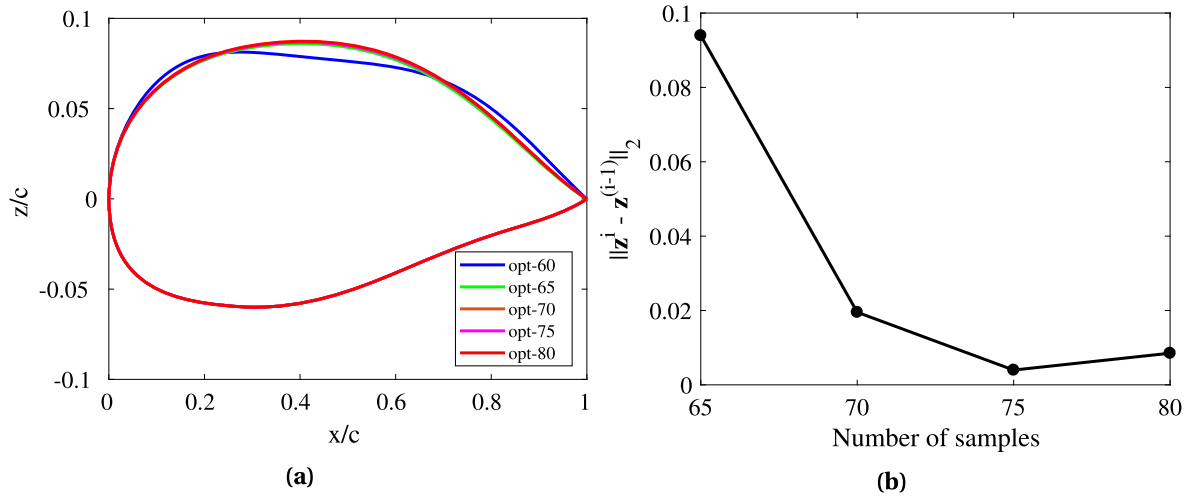
Fig. 9. Evolution of the optimal airfoil shapes: (a) the optimum shapes at the initial surrogate model and at every 5 infill points, and (b) change in z-coordinates of the consecutive optimum designs. (For interpretation of the colors in the figure(s), the reader is referred to the web version of this article.)
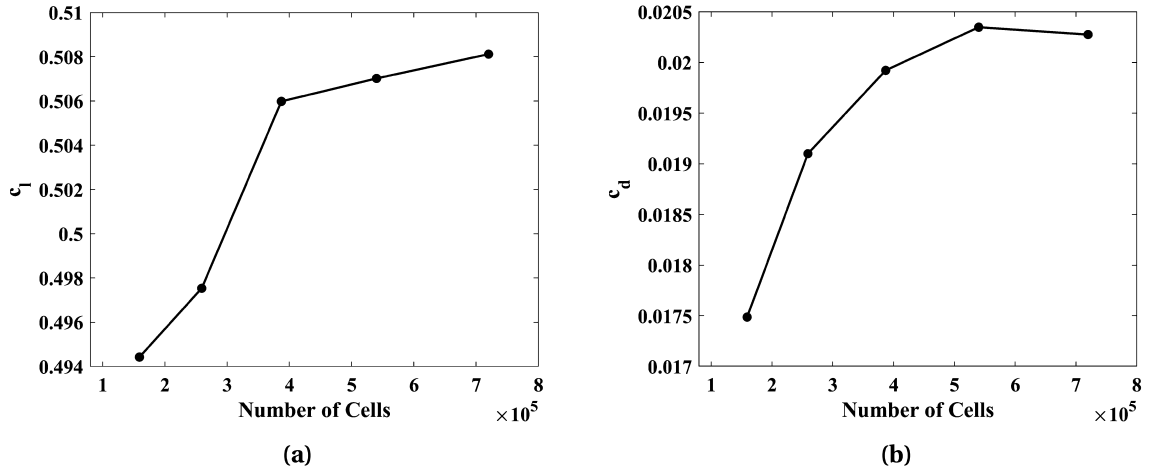

Fig. 10. Results of the grid and time independence study of the optimized shape at Re = 135,000, $\alpha = 4°$ showing the variation in (a) the lift coefficient, and (b) the drag coefficient.
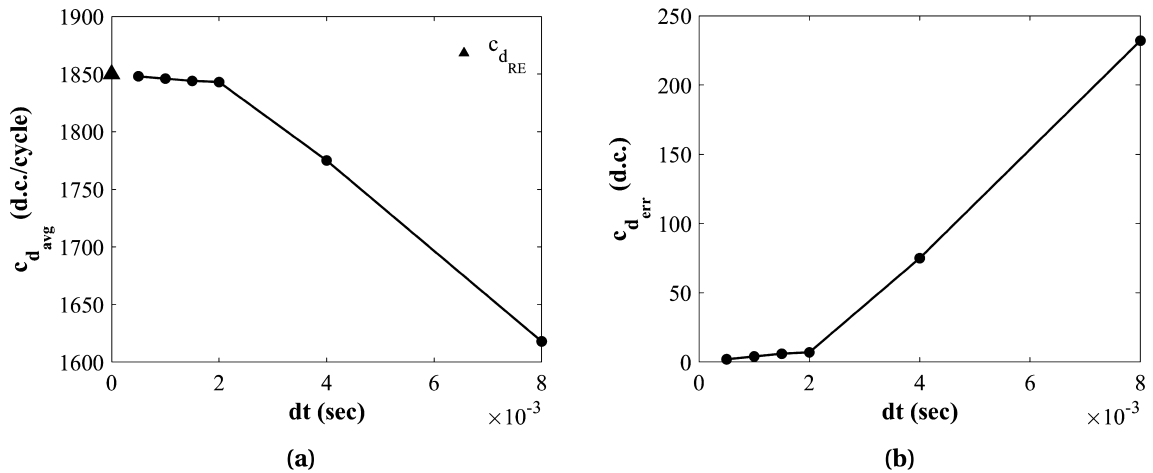

Fig. 11. Results of the time step independence study of optimized design showing (a) the Richardson extrapolation estimate based on the lower order values, and (b) the estimated error from the Richardson extrapolation estimate ($C_{d_{RE}}$).
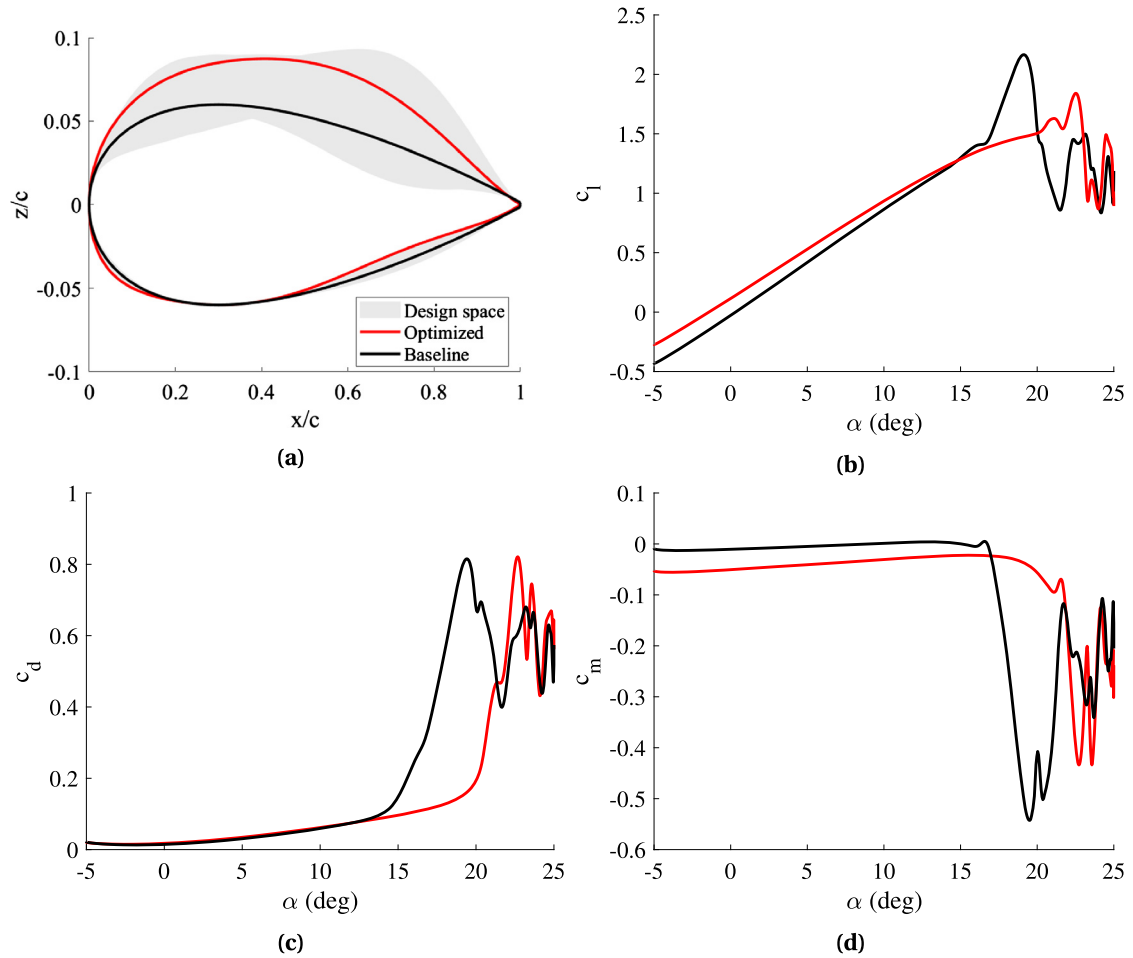
Fig. 12. A comparison of the baseline and optimized designs: (a) airfoil shapes, (b) lift coefficient, (c) drag coefficient, (d) pitching moment coefficient.

Table 6
Properties of the baseline and the optimum airfoil design shapes.

Number of samples	t_{max} *	$x_{t_{max}}$	m_{max} *	$x_{m_{max}}$
Baseline	12	30	0	0
60	14.1	28.8	1.77	69.7
65	14.5	35.1	1.80	62.0
70	14.6	35.1	1.87	62.0
75	14.6	35.1	1.86	62.0
80 (optimum)	14.6	35.3	1.89	62.0

* Shape properties are represented as percentage of the chord length.

with drag count variation within 4 d.c. Thus, considering the simulation time requirement, the mesh with 387,000 cells is still an appropriate mesh. The time study is conducted using the generalized Richardson extrapolation method using the selected mesh with 387,000 cells (see Fig. 11). Richardson's extrapolation estimate of average drag coefficient per cycle is noted to be 1,805 d.c. The time step of 0.0015 s show a reasonable agreement producing $c_{d_{err}} = 6$ d.c. This analysis shows that the mesh with 387,000 cells and a time step of 0.0015 s is still an appropriate selection for producing accurate simulation results for optimized shape.

Fig. 12a shows the shapes of the baseline and the optimized airfoil (opt-80) along with the region covered by possible airfoil shapes in the current design space. The small variation on the lower surface is observed due to the variation in leading-edge radius with assumption ($R_{LE} = R_U = R_L$) (see Section 3.2). The optimized airfoil shape has a larger leading-edge radius, thickness, and camber than the baseline airfoil (see Table 6). In particular, the optimized airfoil has a maximum thickness of $t_{max} = 14.6\%$, which is

larger than the maximum thickness $t_{max} = 12\%$ of the baseline airfoil (see Table 6). Additionally, the location of maximum thickness moves downstream to $x_{t_{max}} = 35.3$ compared to the baseline airfoil which is $x_{t_{max}} = 30$. The optimized airfoil has a maximum camber of $m_{max} = 1.89$ at $x_{m_{max}} = 62.0$ whereas the symmetric baseline airfoil has no camber. The pressure side of the optimized airfoil is also different than the baseline. This difference is majorly due to the airfoil parameterization process where upper and lower surface leading-edge radius are considered equal ($R_{LE} = R_U = R_L$) to get a better understanding at the effect of leading-edge radius on the dynamic stall.

The performance of the optimized shape is evaluated using the CFD model. The aerodynamic characteristics of the baseline and the optimized airfoils in the upstroke pitching cycle are shown in Fig. 12. The lift, drag and pitching moment coefficients of the optimized design shows a delayed dynamic stall when compared to the baseline airfoil. Table 7 gives the details of the dynamic stall cycle for the optimized and the baseline designs.

Figs. 13 and 14 provide Z-vorticity plots for the baseline and the optimized design at angles mentioned in Table 7. As the airfoil undergoes upward pitching motion, lift polar increases for both airfoils. For the baseline airfoil, the lift curve slope increases drastically around $\alpha = 16°$ (Fig. 12b), which is due to an intensification of the DSV and an associated increase in lift. This follows by a moment stall at $\alpha = 16.55°$ for the baseline airfoil (Fig. 12d), which produces a sharp increase in a pitch-down moment due to the DSV propagation (Fig. 13). Additionally, the baseline drag polar shows sudden divergence with the DSV growth and propagation (Fig. 12c). The optimized design shows no signs of the DSV forma-
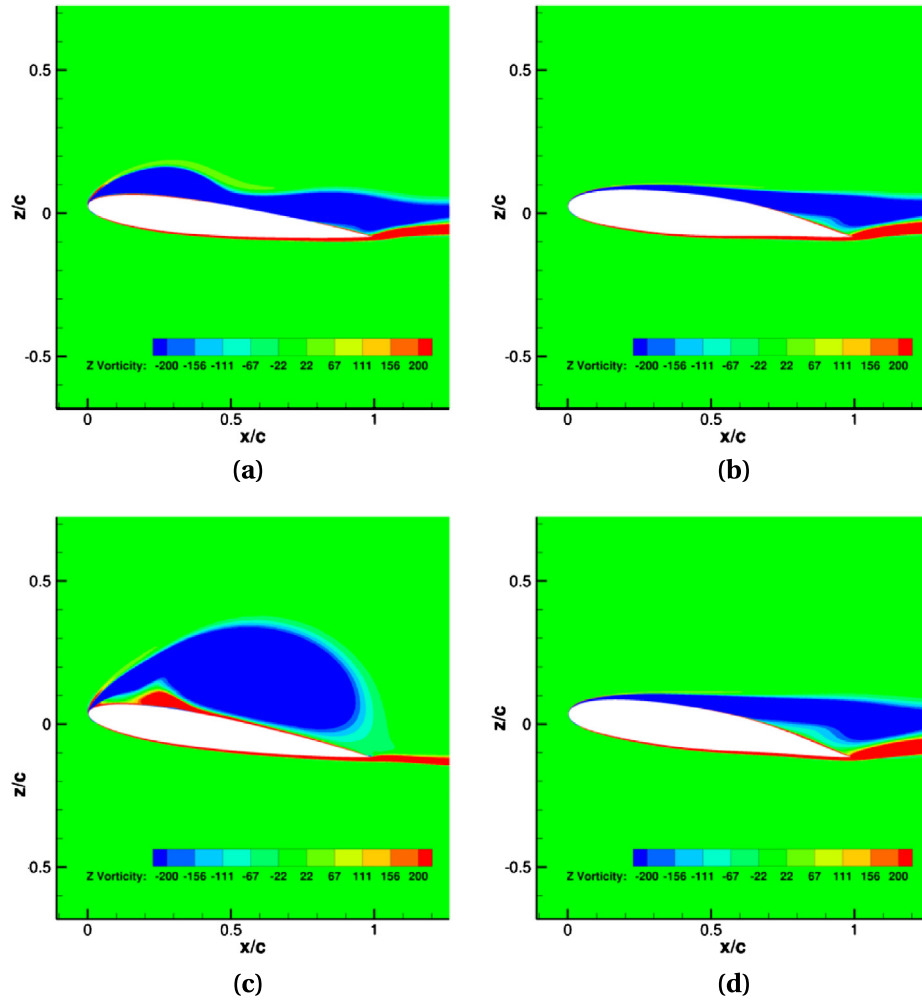
Fig. 13. Z-vorticity contour plot of (a) the baseline at $\alpha = 16.5°$, (b) the optimized shape at $\alpha = 16.5°$, (c) the baseline at $\alpha = 19.1°$, and (d) the optimized shape at $\alpha = 19.1°$.

Table 7
Details of dynamic stall cycle.

Airfoil	α_{ds}	α_{ms}	$c_{l_{max}}$
Baseline (NACA0012)	19.1°	16.5°	2.2
Optimized	22.5°	21.5°	1.8

tion (Fig. 13b) at this angle, and lift continues to increase with the pitch-up motion. However, the trailing edge of the optimized airfoil shows a flow separation moving towards a leading edge. At $\alpha = 19.15°$, the baseline airfoil goes in a dynamic stall as DSV propagates downstream close to the trailing edge and away from the airfoil (Fig. 13c). This causes the lift to drop abruptly, and the baseline airfoil goes in a lift stall. The optimized airfoil shows a slight increase in the pitch-down moment at this angle, with flow separation moving further towards the leading edge (Fig. 13d). As the airfoil pitches further at $\alpha = 21.57°$, the optimized airfoil undergoes a moment stall with a sudden increase in the pitch-down moment and DSV formation (Fig. 14b). It can also be observed that the flow separation from the trailing edge of the optimized design has reached DSV. The baseline airfoil shows a complete flow separation at this angle with strong anticlockwise vortex generating at the trailing edge and a secondary DSV generation at the leading edge (Fig. 14a). The optimized airfoil goes into a dynamic stall at $\alpha = 22.52°$ with DSV detached from the surface near the trailing edge (Fig. 14d).

Further analysis of the stall mechanism of these two airfoils are revealed by plotting the surface flow properties over the suction side of airfoils. Fig. 15 shows contour plots of $-c_p$ and c_f on the suction side of the airfoil as a function of the chord location and angle of attack. This representation is similar to the chord location and time where the angle of attack is a function of time. The sequence of events identified in Figs. 12, 13, and 14 are clearly visible here. As the angle of attack increases, the suction peak on both the airfoils increases near the leading edge, seen by hotspots in Figs. 15a and 15b. The baseline airfoil shows a higher suction peak at lower angle of attack, increasing the adverse pressure gradient much earlier than the optimized airfoil. The higher pressure gradient gives rise to the formation of a separation bubble near the leading edge of both airfoils, represented by the blue-colored region in Figs. 15c and 15d near the leading edge. The increase in the adverse pressure gradient and the formation of a separation bubble is delayed in the optimized airfoil. This could be due to a larger leading edge curvature and thickness. Sharma et al. [88] have reported similar observations for symmetric airfoils with variable thickness.

The formed separation bubble propagates upstream while growing in size with an increase in the angle of attack (see Fig. 15c and 15d). The suction peak suddenly drops, followed by a DSV formation, which occurs at around 15° and 20° for the baseline and the optimized airfoil, respectively. The DSV grows further in size and propagates downstream which is clearly visible in the $-c_p$ plots by the locus of the hotspots or by the black streak running from left to right in the c_f plots (Figs. 15c and 15d). The angle of streak lines indicates the speed at which DSV convects
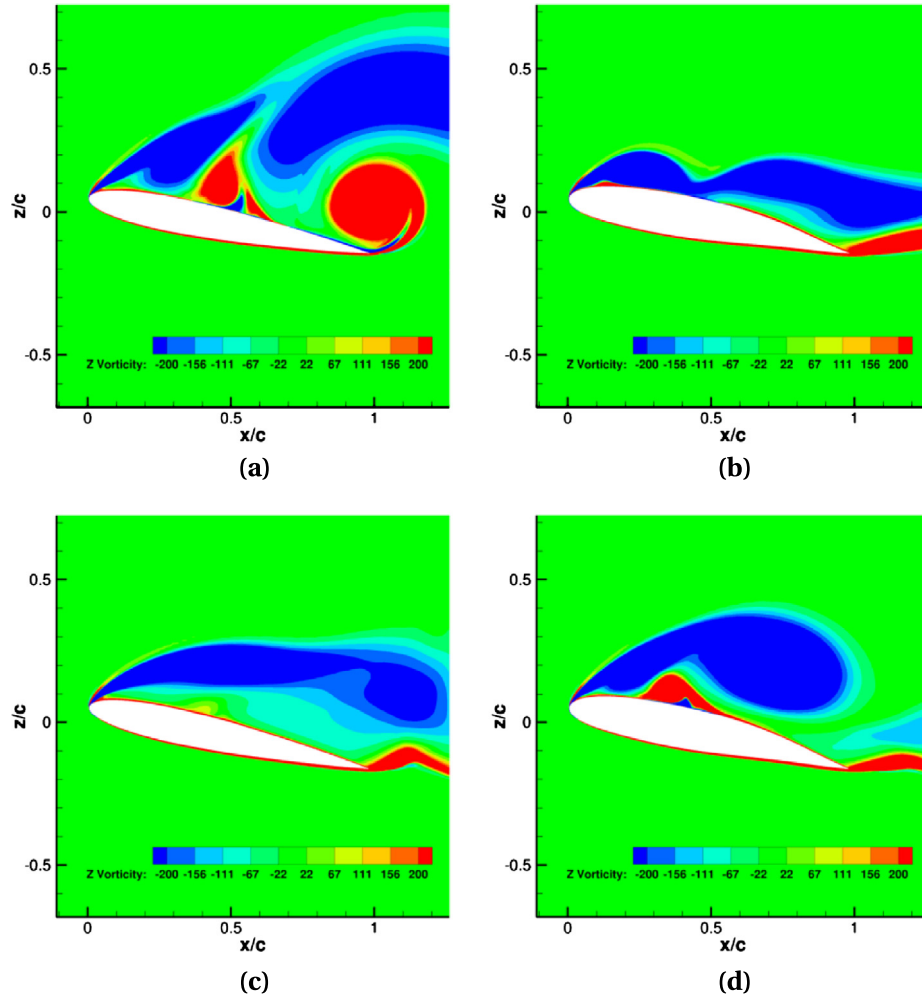
Fig. 14. Z-vorticity contour plot of (a) the baseline at $\alpha = 21.5°$, (b) the optimized shape at $\alpha = 21.5°$, (c) the baseline at $\alpha = 22.5°$, and (d) the optimized shape at $\alpha = 22.5°$.

downstream along the airfoil, whereas the color intensity signifies additional suction induced by the DSV (see Fig. 15c and 15d). It is observed that the DSV convects much faster over the optimized airfoil compared to the baseline with a weak suction trail, mainly due to the deflection of DSV away from the surface as it propagates downstream (see Fig. 14d).

The flow reversal formation near the trailing edge of the airfoils are distinctly different in nature (shown in Figs. 15c and 15d by a blue arrow). The optimized airfoil shows a reversed flow formation from the trailing edge much earlier in the upstroke cycle compared to the baseline. This could be due to a higher thickness and aft camber on the optimized airfoil. Furthermore, this reversed flow moves upstream towards the leading edge with an increase in the angle of attack and reaches the separation bubble at the same time as the DSV is formed for the optimized airfoil. The presence of a flow reversal could be the reason for the low-intensity suction trail left by the DSV for the optimized airfoil since a reversed flow deflects DSV away from the surface as it moves downstream. This upstream flow reversal movement occurs more gradually in the baseline where flow reversal reaches near mid chord when a DSV is formed for the baseline airfoil.

In the baseline design, the DSV is generated from the disturbance in the separation bubble near the leading edge, which is typically categorized as leading-edge stall [25,88]. In contrast, the optimized airfoil shows a trailing edge stall where reversed flow reaches the location of the separation bubble at the same time as the DSV formation.

5.3. Global sensitivity analysis

The surrogate modeling algorithm provides globally accurate models that can be used for the GSA of the objective and constraint functions with respect to the design variables. GSA is performed on the surrogate models using Sobol' indices calculation with the Monte Carlo-based numerical procedure (described in Sec. 3.4) and the LHS sampling technique. The number of samples required for accurate Sobol' indices estimation is selected based on a convergence study. Fig. 16 shows the convergence of S_i and S_{T_i} over the number of samples which indicates their convergence after 10^5 samples. The Sobol' index calculations are repeated 100 times to provide averaged Sobol' index values and their respective standard deviations. The negative signs on Sobol' indices are due to a numerical error in the estimates and are often encountered when the analytical sensitivity indices are close to zero [76].

Fig. 17 shows the averaged GSA results of the objective function with respect to the design variables. The most influential variables are X_U, Z_U, R_{LE}, and Z_{xx_U} in descending order based on their total indices. The variables α_{TE_U} and β_{TE_U} are non-influential to the objective function as their total indices are negligible. These non-influential variables can be fixed in the future for optimization studies as their variations do not affect the objective function. The design variables X_U and Z_U are the most critical variables as their variation directly modifies the airfoil thickness and camber, resulting in the variation of the dynamic stall characteristics.

The difference between the total and the first-order effect $(S_{T_i} - S_i)$ indicates the presence of interaction effects with other
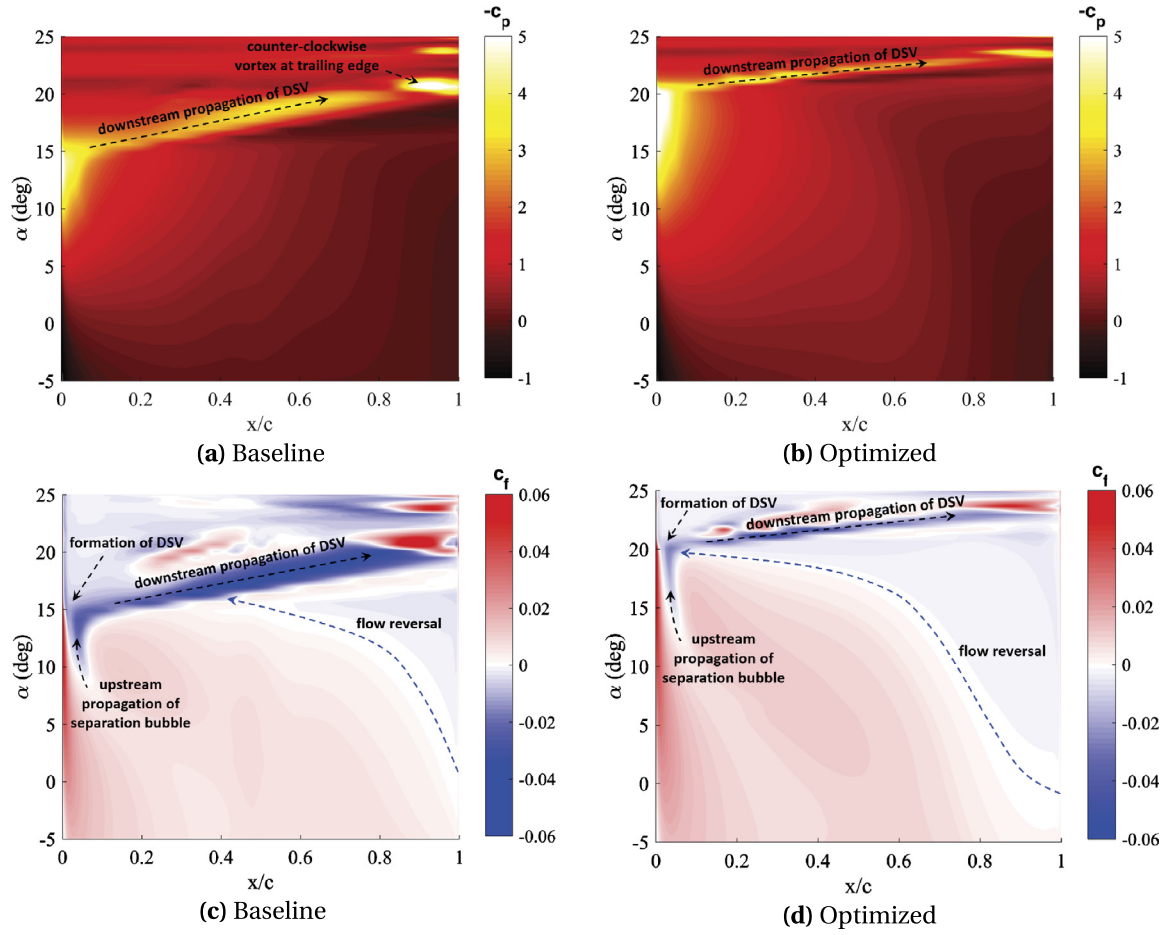
(a) Baseline

(b) Optimized

(c) Baseline

(d) Optimized

Fig. 15. Contours of the pressure coefficient $(-c_p)$ and the skin friction coefficient (c_f) on the suction side for the baseline and optimized airfoils.
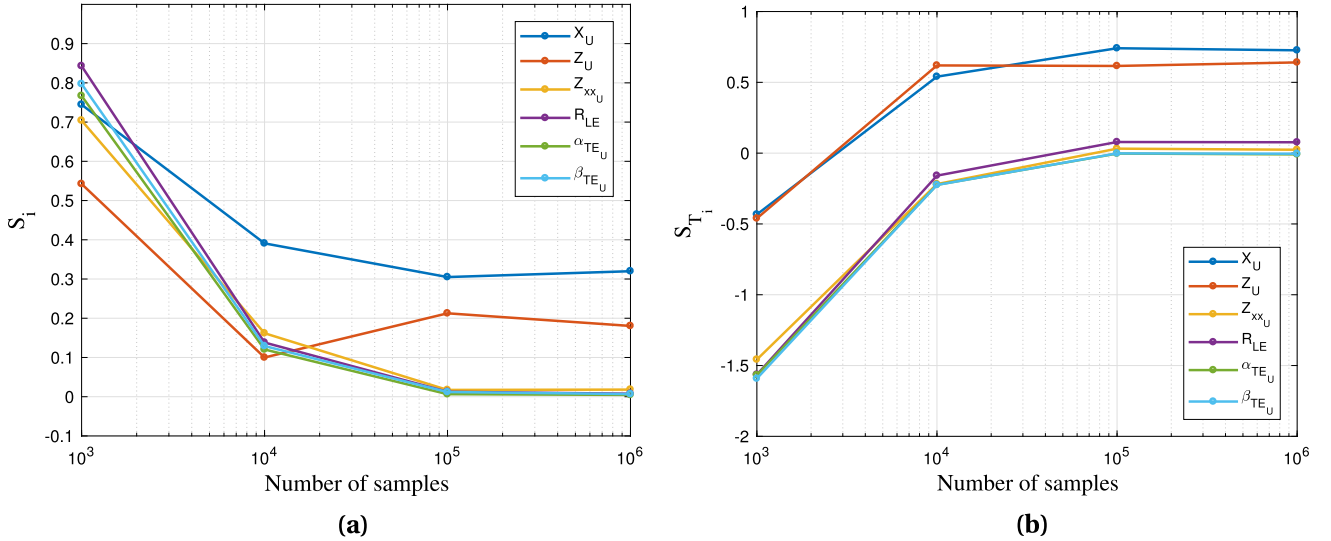

(a)

(b)

Fig. 16. Convergence of the Sobol' indices of the objective function: (a) the first-order Sobol' indices, and (b) the total-effect Sobol' indices.

design variables. The results indicate that the variables X_U and Z_U show the highest interaction effects. The variables Z_U and R_{LE} have comparatively lower first-order effects, but their interactions with other variables moderately affect objective function spread. Furthermore, the magnitude of $1 - \sum_{i=1}^{n} S_i = 0.51$ suggests the interaction among the variables has a larger effect on the objective function spread than their individual first-order effects.

The GSA of the constraint function surrogate model is conducted similarly to the objective function. The constraint function (8) is a function of the dynamic stall angle $(\alpha_{ds}(\mathbf{x}))$ of the airfoil shapes. Thus, the SA of the constraint function surrogate model represents the sensitivity of the design variable to the dynamic stall angle α_{ds} of an airfoil shape. Fig. 18 shows the averaged Sobol' indices results of the constraint function with respect to the design variables. It is observed that the variable Z_U, which changes
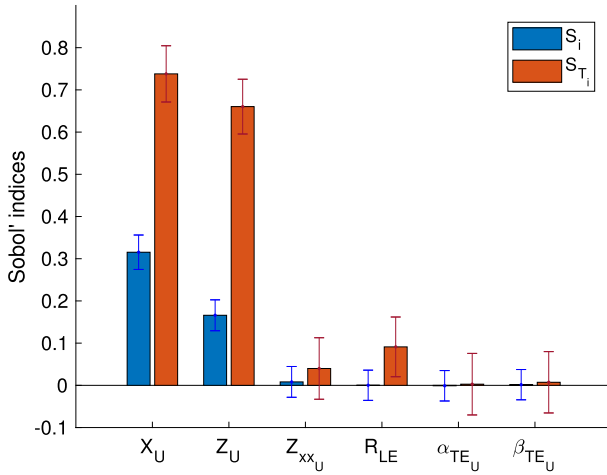
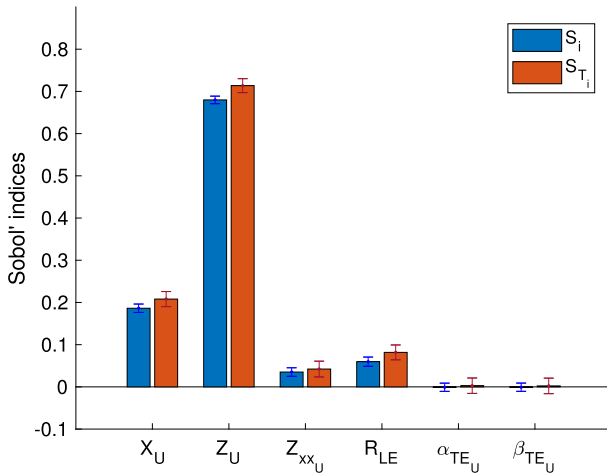**Fig. 17.** Results of global sensitivity analysis of the objective function.

Fig. 18. Results of global sensitivity analysis of the constraint function.

The global sensitivity analysis reveals that the airfoil upper surface thickness and the location of the maximum upper surface thickness are the most influential variables affecting the objective and constraint functions. Moreover, these two variables affect the objective function with a higher interaction effect than their respective first-order effects. The leading-edge radius and the upper surface curvature show a moderate effect on the objective function, whereas the trailing-edge angles showed a negligible effect. Additionally, it is observed that the interaction effects play a more critical role in the objective function than the constraint function.

Although the proposed approach was applied to a wind turbine airfoil shape a similar strategy can be efficiently applied to other aerospace systems, such as rotorcraft, civil transport aircraft, and unmanned air vehicles, to delay or mitigate dynamic stall adverse effects. In future work, this approach will be applied to a complete pitching cycle simulation of a three-dimensional aerodynamic surface undergoing dynamic stall. This would reveal the effects of shape parameters on the aerodynamic coefficients over the entire cycle and the effects on the three-dimensional dynamic stall vortex formation. Additional knowledge on how to mitigate dynamic stall can be revealed by incorporating uncertainties, such as surface tolerances and variation in the freestream speeds, in the optimal design and sensitivity analysis. To further alleviate the computational cost, future work will consider multifidelity methods and dimensionality reduction techniques.

Declaration of competing interest

The authors declare that they have no known competing financial interests or personal relationships that could have appeared to influence the work reported in this paper.

Acknowledgements

This material is based upon work supported by The National Science Foundation under award no. 1739551. The authors would like to thank Dr. Anupam Sharma at Iowa state University, in Ames, Iowa, USA for his guidance in this research.

References

[1] IRENA, Renewable power generation costs in 2018, International Renewable Energy Agency, Abu Dhabi, Tech. Rep., 2019.
[2] N. Ma, H. Lei, Z. Han, D. Zhou, Y. Bao, K. Zhang, L. Zhou, C. Chen, Airfoil optimization to improve power performance of a high-solidity vertical axis wind turbine at a moderate tip speed ratio, Energy 150 (2018) 236–252.
[3] R. Chinchilla, S. Guccione, J. Tillman, Wind power technologies: a need for research and development in improving VAWT's airfoil characteristics, J. Ind. Technol. 27 (1) (2011).
[4] A. Buchner, M. Lohry, L. Martinelli, J. Soria, A. Smits, Dynamic stall in vertical axis wind turbines: comparing experiments and computations, J. Wind Eng. Ind. Aerodyn. 146 (2015) 163–171.
[5] S. Wang, D.B. Ingham, L. Ma, M. Pourkashanian, Z. Tao, Numerical investigations on dynamic stall of low Reynolds number flow around oscillating airfoils, Comput. Fluids 39 (9) (2010) 1529–1541.
[6] J.W. Larsen, S.R. Nielsen, S. Krenk, Dynamic stall model for wind turbine airfoils, J. Fluids Struct. 23 (7) (2007) 959–982.
[7] A. Björck, Dynstall: subroutine package with a dynamic stall model, in: Aeronautical Research Inst. of Sweden, TR-FFAP, vol. 110, 2000.
[8] M.G. Fernández-Godino, C. Park, N.-H. Kim, R.T. Haftka, Review of multi-fidelity models, preprint, arXiv:1609.07196, 2016.
[9] A.I.J. Forrester, A.J. Keane, N.W. Bressloff, Design and analysis of "Noisy" computer experiments, AIAA J. 44 (10) (2006) 2331–2339.
[10] D.R. Jones, M. Schonlau, W.J. Welch, Efficient global optimization of expensive black-box functions, J. Glob. Optim. 13 (4) (1998) 455–492.
[11] T. Rogalsky, R. Derksen, Bézier–PARSEC parameterization for airfoil optimization, Can. Aeronaut. Space J. 55 (3) (2009) 163–174.
[12] D. Peri, F. Tinti, A multistart gradient-based algorithm with surrogate model for global optimization, Commun. Appl. Ind. Math. 3 (1) (2012).
[13] I.M. Sobol, Global sensitivity indices for nonlinear mathematical models and their Monte Carlo estimates, Math. Comput. Simul. 55 (1–3) (2001) 271–280.

the maximum airfoil thickness, prominently affects α_{ds} ($S_T = 0.71$) with minor interaction effects. The variable X_U, which is responsible for variation in the camber location, also substantially affects the dynamic stall angle ($S_T = 0.21$) with very minimal interaction effect. The variables Z_{xx_U} and R_{LE} show minor effects on the α_{ds} spread while α_{TE_U} and β_{TE_U} show negligible effects on α_{ds} and can be fixed for future optimization studies. Overall, the magnitude of $1 - \sum_{i=1}^{n} S_i = 0.04$ indicates that minimal interactions among design variables representing the dynamic stall angle are mostly affected by the design variable individual first-order effects.

6. Conclusion

In this work, a surrogate-based optimization technique to accurately and efficiently delay the dynamic stall adverse effects over an airfoil through aerodynamic shape optimization is proposed. Additionally, global sensitivity analysis is used to reveal the most important shape variables to mitigate the dynamic stall.

The optimal airfoil shape shows a significant delay in the dynamic stall angle and reduction in peak pitching moments compared to the baseline airfoil (NACA 0012). The optimized airfoil has a larger leading-edge radius, higher thickness, and an aft camber. Postoptimality analysis shows that the DSV formation occurs much later for the optimized airfoil compared to the baseline. Moreover, the DSV formed over the optimized airfoil propagates downstream much faster with a weak suction trail producing a lower peak lift coefficient and a gradual moment stall.

18

[14] L.W. Carr, Progress in analysis and prediction of dynamic stall, J. Aircr. 25 (1) (1988) 6–17.

[15] J.M. Brandon, Dynamic stall effects and applications to high performance aircraft, in: Aircraft Dynamics at High Angles of Attack: Experiments and Modelling, 1991.

[16] C.P. Butterfield, Aerodynamic pressure and flow-visualization measurement from a rotating wind turbine blade, Solar Energy Research Inst., Golden, CO (USA), Tech. Rep., 1988.

[17] C. Butterfield, D. Simms, G. Scott, A. Hansen, Dynamic stall on wind turbine blades, National Renewable Energy Lab., Golden, CO (United States), Tech. Rep., 1991.

[18] C.P. Butterfield, Three-Dimensional Airfoil Performance Measurements on a Rotating Wing, Solar Energy Research Institute, 1989.

[19] C.P. Ellington, The novel aerodynamics of insect flight: applications to micro-air vehicles, J. Exp. Biol. 202 (23) (1999) 3439–3448.

[20] C.P. Ellington, C. Van Den Berg, A.P. Willmott, A.L. Thomas, Leading-edge vortices in insect flight, Nature 384 (6610) (1996) 626.

[21] C. Van Den Berg, C.P. Ellington, The vortex wake of a hovering model hawkmoth, Philos. Trans. R. Soc. Lond. B, Biol. Sci. 352 (1351) (1997) 317–328.

[22] J.-Y. Andro, L. Jacquin, Frequency effects on the aerodynamic mechanisms of a heaving airfoil in a forward flight configuration, Aerosp. Sci. Technol. 13 (1) (2009) 71–80.

[23] Y. Hu, H. Zhang, G. Wang, The effects of dynamic-stall and parallel BVI on cycloidal rotor, Aircr. Eng. Aerosp. Technol. 90 (1) (2018) 87–95.

[24] L.W. Carr, K.W. McAlister, W.J. McCroskey, Analysis of the development of dynamic stall based on oscillating airfoil experiments, NASA Technical Note NASA TN D-8382, 1977.

[25] W.J. McCroskey, K. McAlister, L. Carr, S. Pucci, O. Lambert, R. Indergrand, Dynamic stall on advanced airfoil sections, J. Am. Helicopter Soc. 26 (3) (1981) 40–50.

[26] K. McAlister, S. Pucci, W. McCroskey, L. Carr, An experimental study of dynamic stall on advanced airfoil section, Volume 2: pressure and force data, NASA Technical Memorandum 84245, 1982.

[27] W.J. McCroskey, K.W. McAlister, L.W. Carr, S. Pucci, An experimental study of dynamic stall on advanced airfoil sections, Volume 1: summary of the experiment, National Aeronautics and Space Administration, Moffett Field, CA, Ames Research, Tech. Rep., 1982.

[28] Y.H. Yu, S. Lee, K.W. McAlister, C. Tung, C.M. Wang, Dynamic stall control for advanced rotorcraft application, AIAA J. 33 (2) (1995) 289–295.

[29] T. Lee, P. Gerontakos, Dynamic stall flow control via a trailing-edge flap, AIAA J. 44 (3) (2006) 469–480.

[30] H.F. Müller-Vahl, C.N. Nayeri, C.O. Paschereit, D. Greenblatt, Dynamic stall control via adaptive blowing, Renew. Energy 97 (2016) 47–64.

[31] J. Niu, J. Lei, T. Lu, Numerical research on the effect of variable droop leading-edge on oscillating NACA 0012 airfoil dynamic stall, Aerosp. Sci. Technol. 72 (2018) 476–485.

[32] M.G. De Giorgi, V. Motta, A. Suma, Influence of actuation parameters of multi-DBD plasma actuators on the static and dynamic behaviour of an airfoil in unsteady flow, Aerosp. Sci. Technol. 96 (2020) 105587.

[33] H. Zhu, W. Hao, C. Li, Q. Ding, B. Wu, Application of flow control strategy of blowing, synthetic and plasma jet actuators in vertical axis wind turbines, Aerosp. Sci. Technol. 88 (2019) 468–480.

[34] R.M. Hicks, E.M. Murman, G.N. Vanderplaats, An assessment of airfoil design by numerical optimization, NASA, Tech. Rep. NASA-TM-X-3092, 1974.

[35] A. Benaouali, S. Kachel, Multidisciplinary design optimization of aircraft wing using commercial software integration, Aerosp. Sci. Technol. 92 (2019) 766–776.

[36] Z. Lyu, J.R. Martins, Aerodynamic design optimization studies of a blended-wing-body aircraft, J. Aircr. 51 (5) (2014) 1604–1617.

[37] F. Muyl, L. Dumas, V. Herbert, Hybrid method for aerodynamic shape optimization in automotive industry, Comput. Fluids 33 (5–6) (2004) 849–858.

[38] A. Hassanzadeh, A.H. Hassanabad, A. Dadvand, Aerodynamic shape optimization and analysis of small wind turbine blades employing the Viterna approach for post-stall region, Alex. Eng. J. 55 (3) (2016) 2035–2043.

[39] T. Dhert, T. Ashuri, J.R. Martins, Aerodynamic shape optimization of wind turbine blades using a Reynolds-averaged Navier–Stokes model and an adjoint method, Wind Energy 20 (5) (2017) 909–926.

[40] V.S. Vytla, P. Huang, R. Penmetsa, Multi-objective aerodynamic shape optimization of high speed train nose using adaptive surrogate model, in: 28th AIAA Applied Aerodynamics Conference, Chicago, Illinois, July 2010, p. 4383.

[41] A. Samad, K.-Y. Kim, T. Goel, R.T. Haftka, W. Shyy, Multiple surrogate modeling for axial compressor blade shape optimization, J. Propuls. Power 24 (2) (2008) 301–310.

[42] S. Khalfallah, A. Ghenaiet, E. Benini, G. Bedon, Surrogate-based shape optimization of stall margin and efficiency of a centrifugal compressor, J. Propuls. Power 31 (6) (2015) 1607–1620.

[43] A. Jameson, Aerodynamic Shape Optimization Using the Adjoint Method, Lectures at the Von Karman Institute, Brussels, 2003.

[44] J. Laurenceau, M. Meaux, Comparison of gradient and response surface based optimization frameworks using adjoint method, in: 49th AIAA/ASME/ASCE/AHS/ASC Structures, Structural Dynamics, and Materials Conference, 16th AIAA/ASME/AHS Adaptive Structures Conference, 10th AIAA Non-Deterministic Approaches Conference, 9th AIAA Gossamer Spacecraft Forum, 4th AIAA Multidisciplinary Design Optimization Specialists Conference, Schaumburg, IL, April 2008, p. 1889.

[45] R. Lei, J. Bai, D. Xu, Aerodynamic optimization of civil aircraft with wing-mounted engine jet based on adjoint method, Aerosp. Sci. Technol. 93 (2019) 105285.

[46] T. Wong, J.O. Malley, D.O. Brien, Investigation of effect of dynamic stall and its alleviation on helicopter performance and loads, Ann. Forum Proc., Am. Helicopter Soc. 62 (3) (2006) 1749.

[47] S.K. Nadarajah, A. Jameson, Optimum shape design for unsteady flows with time-accurate continuous and discrete adjoint method, AIAA J. 45 (7) (2007) 1478–1491.

[48] K. Mani, B.A. Lockwood, D.J. Mavriplis, Adjoint-based unsteady airfoil design optimization with application to dynamic stall, in: American Helicopter Society 68th Annual Forum Proceedings, vol. 68, American Helicopter Society, Washington, DC, 2012.

[49] Q. Wang, Q. Zhao, Q. Wu, Aerodynamic shape optimization for alleviating dynamic stall characteristics of helicopter rotor airfoil, Chin. J. Aeronaut. 28 (2) (2015) 346–356.

[50] Q. Wang, Q. Zhao, Rotor airfoil profile optimization for alleviating dynamic stall characteristics, Aerosp. Sci. Technol. 72 (2018) 502–515.

[51] Q. Wang, Q. Zhao, Rotor blade aerodynamic shape optimization based on high-efficient optimization method, Proc. Inst. Mech. Eng., G J. Aerosp. Eng. 234 (2) (2020) 375–387.

[52] T. Economon, F. Palacios, J. Alonso, Unsteady aerodynamic design on unstructured meshes with sliding interfaces, in: 51st AIAA Aerospace Sciences Meeting Including the New Horizons Forum and Aerospace Exposition, Grapevine (Dallas/Ft. Worth Region), Texas, January 2013, p. 632.

[53] A. Oyama, S. Obayashi, K. Nakahashi, T. Nakamura, A. Oyama, S. Obayashi, K. Nakahashi, T. Nakamura, Transonic wing optimization using genetic algorithm, in: 13th Computational Fluid Dynamics Conference, Snowmass Village, CO, USA, July 1997, p. 1854.

[54] M.B. Anderson, J. Burkhalter, R. Jenkins, Missile aerodynamic shape optimization using genetic algorithms, J. Spacecr. Rockets 37 (5) (2000) 663–669.

[55] D. Whitley, A genetic algorithm tutorial, Stat. Comput. 4 (2) (1994) 65–85.

[56] D. Quagliarella, A.D. Cioppa, Genetic algorithms applied to the aerodynamic design of transonic airfoils, J. Aircr. 32 (4) (1995) 889–891.

[57] K. Yamamoto, O. Inoue, Applications of genetic algorithm to aerodynamic shape optimization, in: 12th Computational Fluid Dynamics Conference, San Diego, CA, USA, June 1995, p. 1650.

[58] S. Koziel, X.-S. Yang, Computational Optimization, Methods and Algorithms, vol. 356, Springer, 2011.

[59] J. Tang, Y. Hu, B. Song, H. Yang, Unsteady aerodynamic optimization of airfoil for cycloidal propellers based on surrogate model, J. Aircr. 54 (4) (2017) 1241–1256.

[60] G. Persico, A. Romei, V. Dossena, P. Gaetani, Impact of shape-optimization on the unsteady aerodynamics and performance of a centrifugal turbine for ORC applications, Energy 165 (2018) 2–11.

[61] B. Hand, G. Kelly, A. Cashman, Numerical simulation of a vertical axis wind turbine airfoil experiencing dynamic stall at high Reynolds numbers, Comput. Fluids 149 (2017) 12–30.

[62] W. McCroskey, S. Puccif, Viscous-inviscid interaction on oscillating airfoils in subsonic flow, AIAA J. 20 (2) (1982) 167–174.

[63] T. Lee, P. Gerontakos, Investigation of flow over an oscillating airfoil, J. Fluid Mech. 512 (2004) 313–341.

[64] H. Sobieczky, Parametric airfoils and wings, in: Recent Development of Aerodynamic Design Methodologies, Vieweg+Teubner Verlag, Wiesbaden, Germany, 1999, pp. 71–87.

[65] R.M. Hicks, P.A. Henne, Wing design by numerical optimization, J. Aircr. 15 (7) (1978) 407–412.

[66] G. Farin, Curves and Surfaces for Computer-Aided Geometric Design: A Practical Guide, Elsevier, 2014.

[67] T.W. Sederberg, S.R. Parry, Free-form deformation of solid geometric models, in: Proceedings of the 13th Annual Conference on Computer Graphics and Interactive Techniques, Dallas, Texas USA: Association for Computing Machinery, New York, NY, United States, August 1986, pp. 151–160.

[68] M.D. McKay, R.J. Beckman, W.J. Conover, A comparison of three methods for selecting values of input variables in the analysis of output from a computer code, Technometrics 42 (1) (2000) 55–61.

[69] A. Forrester, A. Sobester, A. Keane, Engineering Design via Surrogate Modelling: A Practical Guide, John Wiley & Sons, Wiltshire, Great Britain, 2008.

[70] L. Gu, R. Yang, On reliability-based optimisation methods for automotive structures, Int. J. Mater. Prod. Technol. 25 (1–3) (2006) 3–26.

[71] L. Shi, R. Yang, P. Zhu, A method for selecting surrogate models in crashworthiness optimization, Struct. Multidiscip. Optim. 46 (2) (2012) 159–170.

[72] T.W. Simpson, J. Poplinski, P.N. Koch, J.K. Allen, Metamodels for computer-based engineering design: survey and recommendations, Eng. Comput. 17 (2) (2001) 129–150.

[73] R. Storn, K. Price, Differential evolution—a simple and efficient heuristic for global optimization over continuous spaces, J. Glob. Optim. 11 (4) (1997) 341–359.

[74] P. Virtanen, R. Gommers, T.E. Oliphant, M. Haberland, T. Reddy, D. Cournapeau, E. Burovski, P. Peterson, W. Weckesser, J. Bright, et al., SciPy 1.0–fundamental algorithms for scientific computing in Python, preprint, arXiv:1907.10121, 2019.

[75] L. Lilburne, S. Tarantola, Sensitivity analysis of spatial models, Int. J. Geogr. Inf. Sci. 23 (2) (2009) 151–168.

[76] A. Saltelli, M. Ratto, T. Andres, F. Campolongo, J. Cariboni, D. Gatelli, M. Saisana, S. Tarantola, Global Sensitivity Analysis: The Primer, John Wiley & Sons, West Sussex, England, 2008.

[77] A. Saltelli, Making best use of model evaluations to compute sensitivity indices, Comput. Phys. Commun. 145 (2) (2002) 280–297.

[78] D. Anderson, J.C. Tannehill, R.H. Pletcher, Computational Fluid Mechanics and Heat Transfer, CRC Press, Boca Raton, United States, 2016.

[79] F.R. Menter, Two-equation eddy-viscosity turbulence models for engineering applications, AIAA J. 32 (8) (1994) 1598–1605.

[80] L. Daróczy, G. Janiga, K. Petrasch, M. Webner, D. Thévenin, Comparative analysis of turbulence models for the aerodynamic simulation of h-Darrieus rotors, Energy 90 (2015) 680–690.

[81] F. Palacios, J. Alonso, K. Duraisamy, M. Colonno, J. Hicken, A. Aranake, A. Campos, S. Copeland, T. Economon, A. Lonkar, et al., Stanford university un- structured (SU2): an open-source integrated computational environment for multi-physics simulation and design, in: 51st AIAA Aerospace Sciences Meet- ing Including the New Horizons Forum and Aerospace Exposition, Grapevine (Dallas/Ft. Worth Region), Texas, January 2013, p. 287.

[82] F. Palacios, T.D. Economon, A. Aranake, S.R. Copeland, A.K. Lonkar, T.W. Lukaczyk, D.E. Manosalvas, K.R. Naik, S. Padron, B. Tracey, et al., Stanford uni- versity unstructured (SU2): analysis and design technology for turbulent flows, in: 52nd Aerospace Sciences Meeting, National Harbor, Maryland, 13-17 Jan- uary, 2014, p. 02433.

[83] S. Abbott, Understanding Analysis, Springer, New York, NY, 2001.

[84] OpenFOAM – the open source computational fluid dynamics (CFD) toolbox, http://openfoam.com.

[85] C.J. Roy, Grid convergence error analysis for mixed-order numerical schemes, AIAA J. 41 (4) (2003) 595–604.

[86] Y. Kim, Z.-T. Xie, Modelling the effect of freestream turbulence on dynamic stall of wind turbine blades, Comput. Fluids 129 (2016) 53–66.

[87] D. Kraft, et al., A software package for sequential quadratic programming, Tech. Rep. Report DFVLR-FR 88-28, DLR German Aerospace Center-Institute for Flight Mechanics, Germany, 1988.

[88] A. Sharma, M. Visbal, Numerical investigation of the effect of airfoil thickness on onset of dynamic stall, J. Fluid Mech. 870 (2019) 870–900.